Simulation of acoustic and flexural-gravity waves in ice-covered oceans

Ken Mattsson[a,*], Eric M. Dunham[b], Jonatan Werpers[a]

[a]*Uppsala University, Department of Information Technology, P O Box 337, S-751 05 Uppsala, Sweden*
[b]*Department of Geophysics, Stanford University, Stanford, CA 94305, United States*

Abstract

We introduce a provably stable, high-order-accurate finite difference method for simulation of acoustic and flexural gravity waves in compressible, inviscid fluids partially covered by a thin elastic layer. Such waves arise when studying ocean wave interactions with floating ice shelves, sea ice, and floating structures. Particular emphasis is on a well-posed interface treatment of the fluid-ice coupling. To ensure numerical stability and efficiency, finite difference approximations based on the summation-by-parts (SBP) framework are combined with a penalty technique (simultaneous approximation term, SAT) to impose the boundary and interface conditions. The resulting SBP-SAT approximations are time integrated with an unconditionally stable finite difference method. Numerical simulations in 2D corroborate the predicted efficiency and stability behaviours. The method can be used in its current form to study transmission of ocean waves and tsunamis through ice shelves, and upon coupling to an elastic half-space beneath the ice and water, to study ice motions associated with long-period seismic surface waves.

Keywords: finite difference methods, high-order derivative, high order accuracy, stability, boundary treatment, flexural-gravity waves

1. Introduction

Waves of many kinds occur in Earth's oceans and other bodies of water. These include surface gravity waves and acoustic waves, associated with gravitational restoring forces and fluid compressibility, respectively (e.g., [29, 19, 62]). A floating elastic layer, such as sea ice, an ice shelf, or a thin engineered platform, influences wave propagation, both by providing additional elastic restoring force and by increasing inertia (e.g., [16, 60, 61]). Surface gravity waves, ranging from short wavelength ocean swell to long wavelength tsunamis and tides, become flexural-gravity waves (FGW) in the presence of an elastic layer. In many cases, the layer thickness is small compared to horizontal wavelengths of interest, motivating treatment of the layer through use of an elastic plate model. The classic Euler-Bernoulli plate model, or dynamic beam equation (DBE) in 1D (e.g., [30]), is employed throughout this study. The DBE is a linear partial differential equation (PDE) that is second order in time and fourth order in space. However, for problems involving large strains and rotations, more sophisticated plate models might be used.

Specific motivation for this study comes from the catastrophic disintegration of several Antarctic ice shelves by rifting (e.g., [54, 56, 55, 4, 66]), that is, formation of tensile fractures that cut through the ice shelves and allow infiltration of warm sea water that promotes melting and additional fracturing. It is possible that incident ocean waves, and stresses associated with wave-induced flexure, play some role in creating and/or extending rifts [25, 9, 12, 5]. Recent deployments of seismometers and other instruments have captured the vibrational response of several ice shelves [10, 8, 18, 11], but numerical modeling is required to interpret these data to inform us about ice shelf thickness, elastic properties, and the possible formation

*Corresponding author
Email addresses: ken.mattsson@it.uu.se (Ken Mattsson), edunham@stanford.edu (Eric M. Dunham), jonatan.werpers@it.uu.se (Jonatan Werpers)

of rifts. The data feature not only FGWs, for which the water is effectively incompressible, but also other acoustic and seismic wave modes for which water compressibility is important. This motivates development of a numerical method that accounts for compressibility in addition to the usual physics governing FGWs.

For simplicity, we limit attention in this initial study to the 2D problem with a 1D elastic layer. Several numerical methods exist for this problem, though most are limited to incompressible fluids because of their exclusive focus on FGWs. Sergienko [58, 59] has studied FGWs in the context of ice shelves both analytically and numerically using the COMSOL finite element code. In [58] she considered an ice shelf of arbitrary thickness and solved the 2D quasi-static elasticity equation for the ice shelf (rather than the 1D DBE) coupled to Laplace's equation for the velocity potential in the incompressible water layer. For sufficiently thin ice, her solutions agree well with those utilizing the DBE. Her more recent work [59] again combines analytical solutions with COMSOL numerical simulations, and provides an informative discussion of FGW dispersion characteristics in light of recent observations from the Ross Ice Shelf, West Antarctica.

Papathanasiou et al. [50] also used finite elements to model FGWs, but with the 1D DBE instead of 2D elasticity. The water was again assumed incompressible, but was treated in the context of the shallow-water approximation. Eigenmode expansion methods have also been used for this problem (e.g., [65, 17]).

In contrast to these studies, we account for water compressibility by solving the wave equation instead of Laplace's equation for the velocity potential. This is coupled to the DBE for the ice layer. The coupled equations are solved using a high-order-accurate finite difference method (up to $6th$ order in space). High order methods are exceptionally powerful for wave propagation problems. They allow a considerable reduction in the degrees of freedom, for a given error tolerance. In particular, high-order finite difference methods (HOFDM) are ideally suited for problems of this type. (See the pioneering paper by Kreiss and Oliger [27] concerning hyperbolic problems.) The major difficulty with HOFDM is to obtain a stable boundary treatment, something that has received considerable past attention concerning hyperbolic and parabolic problems. (For examples, see [31, 64, 52, 1, 6, 23].)

A robust and well-proven HOFDM for well-posed initial boundary value problems (IBVP) is obtained by combining summation-by-parts (SBP) operators [26, 63, 37] and either the simultaneous approximation term (SAT) method [13] or the projection method [48, 49, 38, 51] to impose boundary conditions (BC). Recent examples of the SBP-SAT approach can be found in [24, 34, 3, 46, 15, 45, 43]. The SBP operators found in the literature (see for example [26, 63, 37, 41, 42, 14, 2]) are essentially central finite difference stencils, defined on regular grids, closed at the boundaries with a careful choice of one-sided difference stencils, to mimic the underlying integration-by-parts formula in a discrete norm.

The SBP-SAT approach has traditionally been restricted to problems involving first and second derivatives in space. However, there are many problems where higher order derivatives are present. Some examples include the Korteweg-de Vries and the Boussinesq equations (describing nonlinear water waves), soliton models in neuroscience [53], and the Euler-Bernoulli equation for beams [67, 20]. High-order accurate SBP operators for third and fourth derivatives were recently derived [42], and in [44] stable SBP-SAT approximations of the DBE were presented. The main goal in the present study is to formulate a stable and high-order accurate SBP-SAT approximation of a 2D model for ocean acoustic and FGWs in water that is partially covered with ice.

In Section 2 the FGW model is introduced. In Section 3 the SBP-SAT method is introduced. Stability analysis of the 2D problem is presented in Section 4. Time integration is analysed and discussed in Section 5. In Section 6 the accuracy and stability properties of the newly developed SBP-SAT approximations are verified by performing numerical simulations. The code is then applied to study wave reflection/transmission and dispersion of flexural-gravity waves in Section 7. Section 8 summarizes the work.

2. Governing equations

In this study, we consider the 2D problem illustrated in Figure 1. A compressible ocean of depth D is partially covered with an ice shelf. The left domain (denoted $\Omega^{(l)}$) is covered by an ice shelf of length L, with open water of length R in the right domain (denoted $\Omega^{(r)}$). Background on the governing equations and nondimensionalization is provided in Appendix A; in this and the subsequent sections, only

the nondimensional problem is considered. We first analyze the left and right domains separately before moving on to the coupled problem.

The following definitions are used in the subsequent sections:

Definition 2.1. *Let* $\mathbf{x} = (x, y)$ *denote grid coordinates in two dimensions. The* $2D$ *domain is divided into two blocks (left and right), denoted* $\Omega^{(l,r)}$. *We define the left* $2D$ *domain* $-L \leq x \leq 0$, $-D \leq y \leq 0$ *by* $\mathbf{x} \in \Omega^{(l)}$. *Similarly the right* $2D$ *domain* $0 \leq x \leq R$, $-D \leq y \leq 0$ *is denoted by* $\mathbf{x} \in \Omega^{(r)}$. *The right boundary in the left domain, defined by the line* $x = 0$, $-D \leq y \leq 0$, *is denoted* $\delta\Omega_{East}^{(l)}$. *The left boundary in the right domain is denoted* $\delta\Omega_{West}^{(r)}$. *Note that* $\Omega_{East}^{(l)}$ *and* $\Omega_{West}^{(r)}$ *is the shared interface between the two subdomains. Similarly, the top (and bottom) boundaries in the left and right domains are denoted* $\delta\Omega_{Top}^{(l,r)}$ *(and* $\delta\Omega_{Bottom}^{(l,r)}$). *See also Figure 2.*
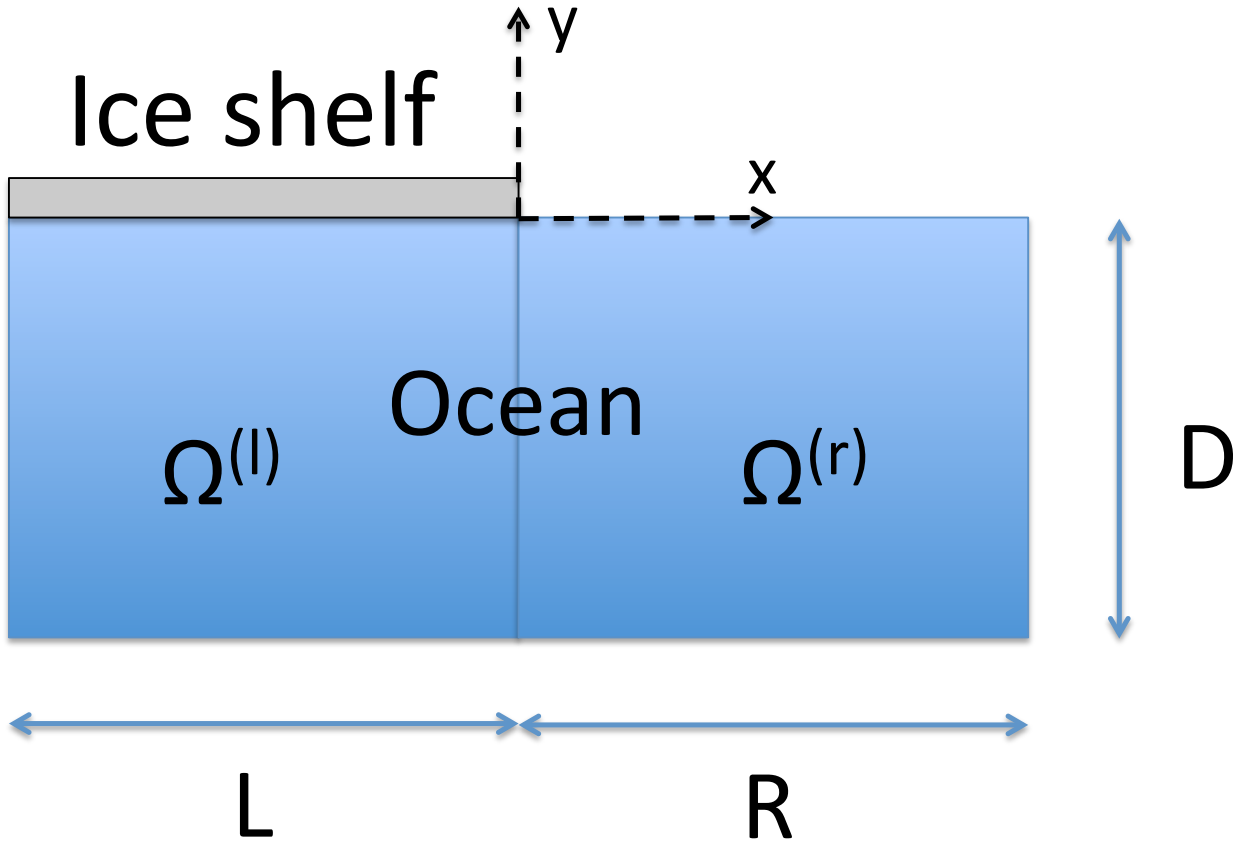

Figure 1: A 2D compressible ocean is partially covered with an ice shelf.

2.1. Left domain (ice-covered), uncoupled

We begin with the left (ice-covered) domain (left side, Figure 1) as a standalone problem, i.e., without coupling to the right (open-water) domain (right side, Figure 1). The nondimensional governing equations, boundary conditions (BCs), and initial conditions for the ice shelf and compressible ocean, as derived in

Appendix A, are

$$aw_{tt} = -bw_{xxxx} - \gamma\phi_t^{(l)}|^0 - w, \quad -L \le x \le 0, \quad t \ge 0,$$
$$w = 0, \ w_x = 0, \qquad\qquad\qquad x = -L, \qquad t \ge 0,$$
$$w_{xx} = 0, \ w_{xxx} = 0, \qquad\qquad\quad x = 0, \qquad\quad t \ge 0,$$
$$w = f_1, \ w_t = f_2, \qquad\qquad\quad -L \le x \le 0, \quad t = 0,$$

$$\tag{1}$$

and

$$\epsilon\phi_{tt}^{(l)} = \phi_{xx}^{(l)} + \phi_{yy}^{(l)}, \qquad \mathbf{x} \in \Omega^{(l)}, \qquad\qquad t \ge 0,$$
$$\phi_x^{(l)} = 0, \qquad\qquad\qquad \mathbf{x} \in \delta\Omega_{West}^{(l)}, \quad t \ge 0,$$
$$\phi_x^{(l)} = 0, \qquad\qquad\qquad \mathbf{x} \in \delta\Omega_{East}^{(l)}, \quad t \ge 0,$$
$$w_t - \phi_y^{(l)} = 0, \qquad\qquad \mathbf{x} \in \delta\Omega_{Top}^{(l)}, \quad t \ge 0,$$
$$\phi_y^{(l)} = 0, \qquad\qquad\qquad \mathbf{x} \in \delta\Omega_{Bottom}^{(l)}, \quad t \ge 0,$$
$$\phi^{(l)} = g_1^{(l)}, \ \phi_t^{(l)} = g_2^{(l)}, \quad \mathbf{x} \in \Omega^{(l)}, \qquad\quad t = 0.$$

$$\tag{2}$$

Here $w(x,t)$ is the vertical displacement of the ice shelf, $\phi^{(l)}(x,y,t)$ is the velocity potential in the ocean in the left domain. (To distinguish between ϕ in the left and right domains we will use the notion $\phi^{(l)}$ and $\phi^{(r)}$, respectively.) In (1), $\phi_t^{(l)}|^0$ denotes $\phi_t^{(l)}$ at the Top (boundary) of the ocean, i.e., the restriction of $\phi_t^{(l)}$ onto $\delta\Omega_{Top}^{(l)}$ (see Figure 2). The horizontal and vertical particle velocities in the ocean are $\phi_x^{(l)}$ and $\phi_y^{(l)}$, respectively, and pressure is $-\gamma\phi_t^{(l)}$. The dimensionless parameters a, b, γ, and ϵ are all non-negative; a quantifies the importance of inertia of the ice and b quantifies the importance of flexural restoring forces. In addition, ϵ quantifies water compressibility effects on flexural-gravity waves, and we can take $\epsilon \to 0$ for incompressible water. When the focus is on FGWs, the problem becomes very stiff because $\epsilon \ll 1$, motivating implicit time stepping.

Remark For the coupled problem (left and right domains) the East BC for $\phi^{(l)}$, here given by $\phi_x^{(l)} = 0$, will be replaced by the interface conditions:

$$\phi^{(l)} = \phi^{(r)}, \ \phi_x^{(l)} = \phi_x^{(r)}, \ x = 0, \ -D \le y \le 0 \ . \tag{3}$$

For the ice shelf we have employed two different types of BC:

$$w = 0, \qquad w_x = 0, \qquad \text{'clamped'},$$
$$w_{xx} = 0, \quad w_{xxx} = 0, \quad \text{'free'},$$

$$\tag{4}$$

with the clamped condition at the West boundary, where the ocean ends and the ice becomes grounded (i.e., attached to the solid bed), and the free condition at the ice shelf edge. [44] provide a thorough analysis of the various BCs for the DBE.

2.2. Right domain (open-water), uncoupled

In the right domain, there is no ice shelf. Therefore we set $a = b = 0$ in equation (1). Hence, we can replace (1) with $\gamma\phi_t^{(r)}|^0 = -w$. We then combine this with the kinematic condition at the top boundary, $w_t = \phi_y^{(r)}|^0$, to eliminate w and obtain the following BC:

$$\gamma\phi_{tt}^{(r)} = -\phi_y^{(r)}, \quad \mathbf{x} \in \delta\Omega_{Top} \ . \tag{5}$$

Remark Instead of imposing (5) at the Top boundary we could have solved for $w = -\gamma \phi_t^{(r)}|^0$ and then used the Top BC $w_t - \phi_y^{(r)}|^0 = 0$.

In the right domain, the combined system given by (1) and (2) is now reduced to

$$
\begin{aligned}
\epsilon \phi_{tt}^{(r)} &= \phi_{xx}^{(r)} + \phi_{yy}^{(r)}, & \mathbf{x} &\in \Omega^{(r)}, & t &\geq 0, \\
\phi_x^{(r)} &= 0, & \mathbf{x} &\in \delta\Omega_{West}^{(r)}, & t &\geq 0, \\
\phi_x^{(r)} &= 0, & \mathbf{x} &\in \delta\Omega_{East}^{(r)}, & t &\geq 0, \\
\gamma \phi_{tt}^{(r)} + \phi_y^{(r)} &= 0, & \mathbf{x} &\in \delta\Omega_{Top}^{(r)}, & t &\geq 0, \\
\phi_y^{(r)} &= 0, & \mathbf{x} &\in \delta\Omega_{Bottom}^{(r)}, & t &\geq 0, \\
\phi^{(r)} = g_1^{(r)}, \ \phi_t^{(r)} &= g_2^{(r)}, & \mathbf{x} &\in \Omega^{(r)}, & t &= 0,
\end{aligned}
\tag{6}
$$

Remark For the coupled problem (left and right domains) the West BC for $\phi^{(r)}$, here given by $\phi_x^{(r)} = 0$, will be replaced by the interface conditions (3).

2.3. Combining the left and right domains

We now couple the left and right domains. The coupling is done only for the ocean, as the ice shelf terminates with a free boundary condition. Hence, (1), (2), and (6) constitute the governing equations for the fully coupled problem, where we have replaced the standalone BC at the shared interface by (3). The main focus is to derive a stable finite difference approximation of these equations.

2.4. Wellposedness

Let the inner product for real-valued functions u, v be defined by $(u,v)_a = \int_{-L}^0 \int_{-D}^0 u^T a\, v \, dxdy$, where $a > 0$ (or $(u,v)_a = \int_{-L}^0 u^T a\, v \, dx$ for the 1D problem). Notice that the definition for the 2D inner product changes with the domain considered, since we also write $(u,v)_a = \int_0^R \int_{-D}^0 u^T a\, v \, dxdy$. The corresponding norm is given by $\|u\|_a^2 = (u,u)_a$.

2.5. Left domain

Multiplying (1) by w_t and integrating by parts twice leads to

$$
\begin{aligned}
(w_t, w_{tt})_a = {} & - w_t b w_{xxx}|_{-L}^0 + (w_{tx}, w_{xxx})_b = \\
& - w_t b w_{xxx}|_{-L}^0 + w_{tx} b w_{xx}|_{-L}^0 - (w_{txx}, w_{xx})_b - (w_t, \phi_t^{(l)}|^0)_\gamma - (w_t, w) \ .
\end{aligned}
$$

Using the clamped and free BC we obtain

$$
\frac{d}{dt} E_{\mathrm{B}} = -2(w_t, \phi_t^{(l)}|^0)_\gamma \ ,
\tag{7}
$$

where the continuous energy E_{B} in the beam is given by

$$
E_{\mathrm{B}} = \|w_t\|_a^2 + \|w_{xx}\|_b^2 + \|w\|^2 \ .
\tag{8}
$$

For E_{B} to be an energy it is required that $E_{\mathrm{B}} \geq 0$, which implies that a and b have to be non-negative, all in accordance with the underlying physics.

Multiplying (2) by $\gamma \phi_t^{(l)}$, integrating by parts, and using the BCs leads to

$$
\begin{aligned}
(\phi_t^{(l)}, \phi_{tt}^{(l)})_{\gamma\epsilon} =& \gamma \int_{-D}^0 \phi_t^{(l)} \, \phi_x^{(l)}|_{-L}^0 \, dy + \gamma \int_{-L}^0 \phi_t^{(l)} \, \phi_y^{(l)}|_{-D}^0 \, dx \\
& - (\phi_{tx}^{(l)}, \phi_x^{(l)})_\gamma - (\phi_{ty}^{(l)}, \phi_y^{(l)})_\gamma \\
& \Downarrow \\
& \frac{d}{dt} E_{\mathrm{O}}^{(l)} = 2\gamma \int_{-L}^0 \phi_t^l \, w_t|^0 \, dx \, ,
\end{aligned}
\tag{9}
$$

where the continuous energy $E_{\mathrm{O}}^{(l)}$ in the ocean is given by

$$
E_{\mathrm{O}}^{(l)} = \|\phi_t^{(l)}\|_{\epsilon\gamma}^2 + \|\phi_x^{(l)}\|_\gamma^2 + \|\phi_y^{(l)}\|_\gamma^2 \, .
\tag{10}
$$

By combining (7) and (9) we obtain,

$$
\frac{d}{dt} E^{(l)} = 0 \, ,
\tag{11}
$$

where the continuous energy (in the left domain) is given by

$$
E^{(l)} = E_{\mathrm{B}} + E_{\mathrm{O}}^{(l)} = \|w_t\|_a^2 + \|w_{xx}\|_b^2 + \|w\|^2 + \|\phi_t^{(l)}\|_{\epsilon\gamma}^2 + \|\phi_x^{(l)}\|_\gamma^2 + \|\phi_y^{(l)}\|_\gamma^2 \, .
\tag{12}
$$

(Here we have used the fact that $\gamma \int_{-L}^0 \phi_t^{(l)} \, w_t|^0 \, dx = (w_t, \phi_t^{(l)}|^0)_\gamma$.) Hence, the total energy, given by (12), is conserved.

2.6. Right domain

We now turn to the right domain, where there is no ice shelf, i.e., the model given by (6). The energy method applied to (6) yields

$$
\begin{aligned}
(\phi_t^{(r)}, \phi_{tt}^{(r)})_{\gamma\epsilon} =& \gamma \int_{-D}^0 \phi_t^{(r)} \, \phi_x^{(r)}|_0^R \, dy + \gamma \int_0^R \phi_t^{(r)} \, \phi_y^{(r)}|_{-D}^0 \, dx \\
& - (\phi_{tx}^{(r)}, \phi_x^{(r)})_\gamma - (\phi_{ty}^{(r)}, \phi_y^{(r)})_\gamma \\
& \Downarrow \\
& \frac{d}{dt} E^{(r)} = 0 \, ,
\end{aligned}
\tag{13}
$$

where the continuous energy (in the right domain) is given by

$$
E^{(r)} = \int_0^R (\gamma \phi_t^{(r)})^2|^0 \, dx + \|\phi_t^{(r)}\|_{\epsilon\gamma}^2 + \|\phi_x^{(r)}\|_\gamma^2 + \|\phi_y^{(r)}\|_\gamma^2 \, .
\tag{14}
$$

Here we can use the relation, $\gamma \phi_t|^0 = -w$ to replace $\int_0^R (\gamma \phi_t^{(r)})^2|^0 \, dx$ with $\|w\|^2$ in (14). Hence, $E^{(r)}$ is completely analogous to $E^{(l)}$ if we set $a = b = 0$.

2.7. Combining the left and right domains

The energy estimate for the combined system, given by (1), (2), and (6), where we have replaced the standalone BC at the shared interface by (3), is given by

$$
\frac{d}{dt} \left(E^{(l)} + E^{(r)} \right) = 0 \, .
\tag{15}
$$

As before, total energy is conserved, but now it can be exchanged between the left and right domains through the common interface.

3. The finite difference method in 1D

In an effort of making the stability analysis of the fully coupled problem easier to follow, we start by introducing the SBP-SAT finite difference methodology for the 1D uncoupled DBE. In Section 4 we extend the stability analysis to the fully coupled 2D problem. First some definitions are needed.

3.1. Definitions

The following definitions are needed later in the study. The domain $(-L \leq x \leq 0)$ is discretized using the following m equidistant grid points:

$$x_i = -L + (i-1)\,h_x, \quad i = 1, 2, \ldots, m, \quad h_x = \frac{L}{m-1} \ .$$

The approximate solution at grid point x_i is denoted v_i, and the discrete solution vector is $v^T = [v_1, v_2, \ldots, v_m]$. Similarly, we define an inner product for discrete real-valued vector functions $w, v \in \mathbf{R^m}$ by $(w, v)_H = w^T H\,v$, where H is positive definite. The corresponding norm is $\|v\|_H^2 = v^T H\,v$.

Definition 3.1. *To simplify notation we will write v_t for the time-derivative of the discrete solution vector, i.e., $\frac{d\,v}{dt}$.*

The following vectors will be frequently used:

$$e_1 = [1, 0, \ldots, 0]^T, \quad e_m = [0, \ldots, 0, 1]^T \ . \tag{16}$$

The following definition (first stated in [40, 36]) is central to the present study:

Definition 3.2. *An explicit $2p$th-order accurate finite difference scheme with minimal stencil width for the Cauchy problem is denoted a $2p$th-order accurate narrow-stencil.*

3.2. SBP operator

SBP operators are essentially central finite difference stencils closed at the boundaries with a careful choice of one-sided difference stencils, to mimic the integration-by-parts formula in a discrete inner product. In the present paper we address the SBP operators by the accuracy of the central scheme and the type of norm which they are based on. In the present study we focus on diagonal-norm SBP operators. The definitions for first- and second-derivative SBP operators can be found in earlier papers (see for example [13, 37, 40, 36, 35, 39, 41]). In a recent paper [42] third- and fourth-derivative SBP operators were derived.

The following SBP definition (first introduced in [36]) is central to the present study:

Definition 3.3. *A difference operator $D_2^{(b)} = H^{-1}(-M^{(b)} + b_m e_m d_{1;m} - b_1 e_1 d_{1;1})$ approximating $\partial/\partial\,x\,(\,b\,\partial/\partial\,x)$, where $b > 0$, using a $2p$th-order accurate narrow-stencil in the interior, is said to be a $2p$th-order diagonal-norm second-derivative SBP operator if the diagonal matrix H defines a discrete norm, $M^{(b)} = (M^{(b)})^T \geq 0$, $d_{1;1}$ and $d_{1;m}$ are first derivative finite difference stencils at x_1 and x_m.*

The vectors e_1 and e_m are defined in (16). Diagonal-norm second-derivative SBP operators of orders 2, 4 and 6 were derived in [41]. For the constant coefficient case $D_2^{(b)} = b\,D_2$ where D_2 is an approximation of $\partial^2/\partial\,x^2$. High-order accurate D_2 operators were derived in [37]. The following lemma (first introduced in [36]) is relevant to the present study:

Lemma 3.4. *The dissipative part $M^{(b)}$ of a narrow-diagonal second-derivative SBP operator has the following property:*

$$v^T M^{(b)} v = h\,\frac{\alpha_1}{b_1}(d_{1;1}v)^2 + h\,\frac{\alpha_1}{b_m}(d_{1;m}v)^2 + v^T \tilde{M}^{(b)} v \ , \tag{17}$$

where $\tilde{M}^{(b)}$ is symmetric and positive semi-definite, and α_1 a positive constant, independent of h.

7

second-order	fourth-order	sixth-order
1	0.2508560249	0.1878715026

Table 1: α_1 in Eq. 17 for the second-, fourth- and sixth-order accurate diagonal-norm second-derivative SBP operators.

For the special but important case of constant coefficients ($b = 1$) the numerically derived values of α_1 for the second-, fourth- and sixth-order accurate finite difference SBP operators (presented in Appendix B) are presented in Table 1.

For completeness we restate (first introduced in [42]) the definition of a fourth-derivative SBP operator:

Definition 3.5. *A difference operator*
$D_4 = H^{-1} \left(N - e_1 d_{3;1} + e_m d_{3;m} + d_{1;1}^T d_{2;1} - d_{1;m}^T d_{2;m} \right)$ *approximating* $\partial^4 / \partial x^4$, *using a 2pth-order accurate narrow-stencil in the interior, is said to be a 2pth-order diagonal-norm fourth-derivative SBP operator if $H = H^T > 0$ is diagonal, $N = N^T \geq 0$, $d_{1;1}$ and $d_{1;m}$ are first derivative finite difference stencils at x_1 and x_m, $d_{2;1}$ and $d_{2;m}$ are second derivative finite difference stencils at x_1 and x_m, and $d_{3;1}$, $d_{3;m}$ are third derivative finite difference stencils at x_1 and x_m.*

The SBP operators are presented in Appendix B. For further details concerning the various SBP operators we refer to [42].

The following two lemmas first presented in [44] are relevant to the present study:

Lemma 3.6. *The dissipative part N of a diagonal-norm fourth-derivative SBP operator has the following property:*

$$v^T N v = h\,\alpha_2 \left((d_{2;1} v)^2 + (d_{2;m} v)^2 \right) + v^T \tilde{N}_2 v \,, \tag{18}$$

where $\tilde{N}_2$ is symmetric and positive semi-definite, and α_2 a positive constant, independent of h.

Lemma 3.7. *The dissipative part N of a diagonal-norm fourth-derivative SBP operator has the following property:*

$$v^T N v = h^3\,\alpha_3 \left((d_{3;1} v)^2 + (d_{3;m} v)^2 \right) + v^T \tilde{N}_3 v \,, \tag{19}$$

where $\tilde{N}_3$ is symmetric and positive semi-definite, and α_3 a positive constant, independent of h.

The values of α_2 and α_3, were derived numerically for the second-, fourth- and sixth-order accurate finite difference SBP discretizations. The results are presented in Table 2.

$\alpha_2^{(2nd)}$	$\alpha_2^{(4th)}$	$\alpha_2^{(6th)}$	$\alpha_3^{(2nd)}$	$\alpha_3^{(4th)}$	$\alpha_3^{(6th)}$
1.250	0.505	0.325	0.4	0.928	0.158

Table 2: $\alpha_{2,3}$ in Eqs. 18 and 19, for the second-, fourth- and sixth-order accurate diagonal-norm fourth-derivative SBP operators.

3.3. The SBP-SAT method

The semi-discrete approximation of the ice shelf BC given by (4) can be written as

$$
\begin{aligned}
e_1^T w = 0, \qquad d_{1;1} w = 0, &\quad \text{'clamped'}\,, \\
d_{2;m} w = 0, \quad d_{3;m} w = 0, &\quad \text{'free'}\,.
\end{aligned}
\tag{20}
$$

The SBP-SAT approximation of (1) is given by

$$
\begin{aligned}
a w_{tt} = {} & -b\, D_4 w - \gamma e_{Top}^T v_t^{(l)} - w + b\, H^{-1}(d_{3;1} - \tau_1 e_1^T)^T \left(e_1^T w - 0\right) \\
& - b\, H^{-1}(d_{2;1} + \tau_2 d_{1;1})^T \left(d_{1;1} w - 0\right) \\
& - \sigma_1 H^{-1} d_{1;m}^T \left(d_{2;m} w - 0\right) \\
& + \sigma_2 H^{-1} e_m \left(d_{3;m} w - 0\right) \ ,
\end{aligned}
\tag{21}
$$

where $e_{Top}^T v_t^{(l)}$ is an approximation of $\phi_t^{(l)}|^0$ (see (22) and (24)). Here $\tau_{1,\,2}$ and $\sigma_{1,\,2}$ are penalty parameters chosen to obtain a semi-discrete energy estimate. (For the stability analysis of (21), the coupling to the ocean governed by $\gamma e_{Top}^T v_t^{(l)}$, can be considered a known forcing function.)

The following lemma is important in the present study:

Lemma 3.8. *Eq. 21 is stable if D_4 is a diagonal-norm fourth-derivative SBP operator, $\tau_1 \geq \frac{2}{h^3 \alpha_3}$, $\tau_2 \geq \frac{2}{h \alpha_2}$ and $\sigma_1 = \sigma_2 = -b$ hold.*

Proof Multiplying (21) by $w_t^T H$, and adding the transpose leads to

$$
\begin{aligned}
\frac{d}{dt} & \left(a \, \|w_t\|_H^2 + b\, w^T N w + \|w\|_H^2\right) = -2\gamma w_t^T H e_{Top}^T v_t^{(l)} \\
& + b\, \frac{d}{dt}\left((w_1) d_{3;1} w - (d_{1;1} w) d_{2;1} w - \tau_1 w_1^2 - \tau_2 (d_{1;1} w)^2\right) \\
& + 2(b + \sigma_1)(d_{1;m} w_t) d_{2;m} w - 2(b + \sigma_2)(w_t)_m d_{3;m} w \ .
\end{aligned}
$$

Choosing $\sigma_1 = \sigma_2 = -b$ while using the fact that D_4 is a diagonal-norm fourth-derivative SBP operator we obtain

$$
\frac{d}{dt} \bar{E}_{\mathrm{B}} = -2\gamma w_t^T H e_{Top}^T v_t^{(l)},
$$

where

$$
\bar{E}_{\mathrm{B}} = a \, \|w_t\|_H^2 + b\, w^T N w + \|w\|_H^2 + b\, \tilde{w}_1^T A_1 \tilde{w}_1 \ ,
$$

and

$$
\tilde{w}_1 = \begin{bmatrix} w_1 \\ d_{1;1} w \\ d_{2;1} w \\ d_{3;1} w \end{bmatrix}, \qquad
A_1 = \begin{bmatrix} \tau_1 & 0 & 0 & -1 \\ 0 & \tau_2 & 1 & 0 \\ 0 & 1 & 0 & 0 \\ -1 & 0 & 0 & 0 \end{bmatrix}.
$$

To establish $\bar{E}_{\mathrm{B}}$ as an energy we need to show that $\bar{E}_{\mathrm{B}} \geq 0$. Using Lemmas 3.6, 3.7 we have

$$
\bar{E}_{\mathrm{B}} \geq b w^T N w + b\, \tilde{w}_1^T A_1 \tilde{w}_1 \geq \frac{1}{2} w^T \left(\tilde{N}_2 + \tilde{N}_3\right) w + b\, \tilde{w}_1^T \tilde{A}_1 \tilde{w}_1 \geq b\, \tilde{w}_1^T \tilde{A}_1 \tilde{w}_1
$$

where

$$
\tilde{A}_1 = \begin{bmatrix} \tau_1 & 0 & 0 & -1 \\ 0 & \tau_2 & 1 & 0 \\ 0 & 1 & \frac{h}{2}\alpha_2 & 0 \\ -1 & 0 & 0 & \frac{h^3}{2}\alpha_3 \end{bmatrix}.
$$

By choosing $\tau_1 \geq \frac{2}{h^3 \alpha_3}$, $\tau_2 \geq \frac{2}{h \alpha_2}$, $\tilde{A}_1$ is positive semi-definite and $\bar{E}_{\mathrm{B}} \geq 0$, thus defining a semi-norm. Therefore the scheme is stable with the following discrete energy estimate,

$$
\frac{d}{dt} \bar{E}_{\mathrm{B}} = -2\gamma w_t^T H e_{Top}^T v_t^{(l)},
$$

which mimics the corresponding continuous energy estimate (8) in the ice shelf. $\square$

Remark The term $b\,w^T N w$ is a discrete analog of $b\,\|w_{xx}\|_b^2$ in the continuous energy, while $b\,\tilde{w}_1^T A_1 \tilde{w}_1$ is a $\mathcal{O}(h^p)$ correction due the boundary conditions.

4. The finite difference method in 2D

We will here extend the SBP-SAT methodology to 2D, in order to discretize the coupled system in the ocean given by (2) and (6) with the interface coupling (3).

4.1. Definitions

To simplify the 2D analysis we introduce some notation, beginning with the Kronecker product:

$$
C \otimes D = \begin{bmatrix} c_{1,1}\,D & \cdots & c_{1,q}\,D \\ \vdots & & \vdots \\ c_{p,1}\,D & \cdots & c_{p,q}\,D \end{bmatrix} ,
$$

where C is a $p \times q$ matrix and D is an $m \times n$ matrix. Two useful rules for the Kronecker product are $(A \otimes B)(C \otimes D) = (AC) \otimes (BD)$ and $(A \otimes B)^T = A^T \otimes B^T$.

The left domain $\Omega^{(l)}$ is discretized with an $(m_x + 1) \times (m_y + 1)$-point equidistant grid defined as

$$
x_i = -L + (i-1)h_x, \quad i = 1, 2, \ldots, m_x, \quad h_x = \tfrac{L}{m_x - 1},
$$

$$
y_j = -D + (j-1)h_y, \quad j = 1, 2, \ldots, m_y, \quad h_y = \tfrac{D}{m_y - 1}.
$$

The numerical approximation at grid point $(x_i,\, y_j)$ is denoted $v_{i,j}^{(l)}$. (The grid for the right domain is defined analogously and we will use $v^{(r)}$ to denote the solution vector.)

The tensor product derivations are more transparent if we redefine the component vector $v_{i,j}$ as a "vector of vectors." Specifically, define a discrete solution vector $v^T = [v^1, v^2, \ldots, v^{m_x}]$, where $v^p = [v_{p,1}, v_{p,2}, \ldots, v_{p,m_y}]$ is the solution vector at x_p along the y-direction, see Figure 2. To distinguish whether a 2D difference operator P is operating in the x- or the y-direction, we use the notations P_x and P_y, respectively. The following 2D operators are frequently used:

$$
\begin{aligned}
D_{2x} &= D_2 \otimes I_{m_y}, & D_{2y} &= I_{m_x} \otimes D_2, \\
H_x &= H \otimes I_{m_y}, & H_y &= I_{m_x} \otimes H, \\
e_{West} &= e_1 \otimes I_{m_y}, & e_{Bottom} &= I_{m_x} \otimes e_1, \\
e_{East} &= e_{m_x} \otimes I_{m_y}, & e_{Top} &= I_{m_x} \otimes e_{m_y}, \\
d_{1;West} &= d_{1;1} \otimes I_{m_y}, & d_{1;Bottom} &= I_{m_x} \otimes d_{1;1}, \\
d_{1;East} &= d_{1;m} \otimes I_{m_y}, & d_{1;Top} &= I_{m_x} \otimes d_{1;m},
\end{aligned} \tag{22}
$$

where D_2 and H are the 1D operators introduced in Section 3. I_{m_x} and I_{m_y} are identity matrices of appropriate sizes, and $d_{1;1}$, $d_{1;m}$, e_1, e_{m_x} and e_{m_y} are 1D "boundary" vectors defined by (16) and Definition 3.3. We further introduce the 2D norm operator $\bar{H} = H_x H_y$. $e_{Top}^T v$ corresponds to the solution vector at the Top boundary.

4.2. Stability analysis in the ocean

In this section we present the SBP-SAT approximations of (2) and (6), with the interface coupling (3).

The semi-discrete approximation of the continuity conditions (3) can be written

$$
I_1 \equiv e_{East}^T v^{(l)} - e_{West}^T v^{(r)} = 0 , \quad I_2 \equiv d_{1;East} v^{(l)} - d_{1;West} v^{(r)} = 0 , \tag{23}
$$

where $v^{(l,r)}$ are the solution vectors corresponding to the left and right domains respectively. The left and right domains are discretized using m_y grid points along the shared interface (at $x = 0$).
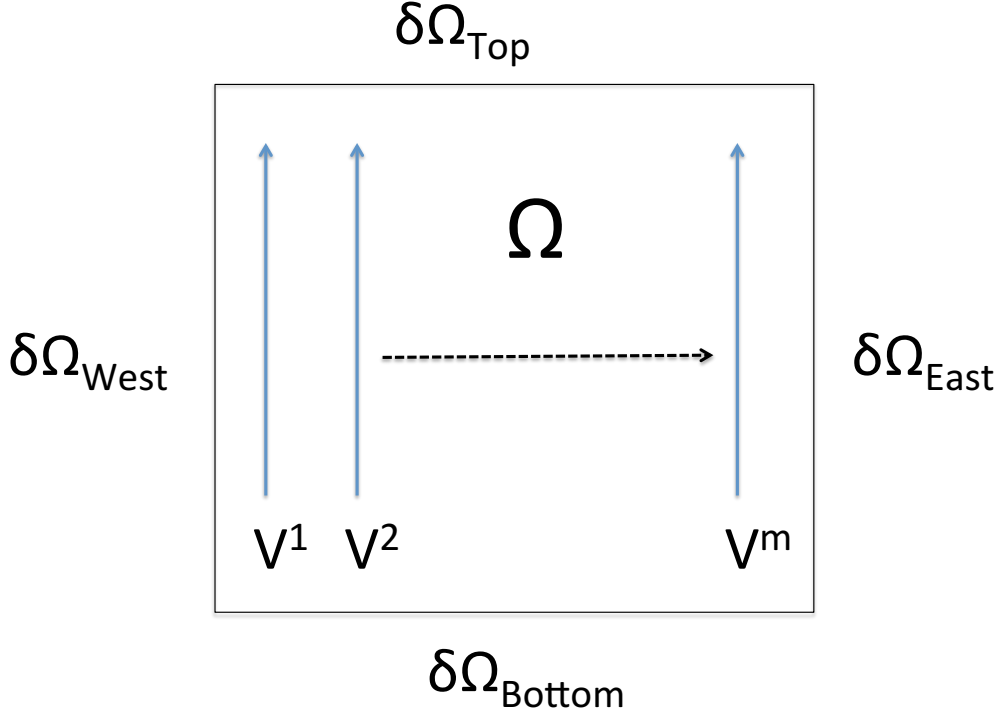
Figure 2: Domain 2D.

The SBP-SAT method for (2) and (6) with the interface coupling (3) is given by

$$
\begin{aligned}
&\epsilon v_{tt}^{(l)} = D_{2x} v^{(l)} + D_{2y} v^{(l)} && \epsilon v_{tt}^{(r)} = D_{2x} v^{(r)} + D_{2y} v^{(r)} \\
&+\tau H_x^{-1} e_{East}(I_1) && -\tau H_x^{-1} e_{West}(I_1) \\
&+\sigma H_x^{-1} d_{1;East}^T(I_1) && +\sigma H_x^{-1} d_{1;West}^T(I_1) \\
&+\beta H_x^{-1} e_{East}(I_2) && +\beta H_x^{-1} e_{West}(I_2) \\
&+H_x^{-1} e_{West}(d_{1;West} v^{(l)}) && -H_x^{-1} e_{East}(d_{1;East} v^{(r)}) \\
&+H_y^{-1} e_{Bottom}(d_{1;Bottom} v^{(l)}) && +H_y^{-1} e_{Bottom}(d_{1;Bottom} v^{(r)}) \\
&+H_y^{-1} e_{Top}(w_t - d_{1;Top} v^{(l)}) && -H_y^{-1} e_{Top}(\gamma e_{North} v_{tt}^{(r)} + d_{1;Top} v^{(r)})
\end{aligned}
\tag{24}
$$

The following lemma is central in the present study:

Lemma 4.1. *The scheme (24) is stable if D_2 is a diagonal-norm second-derivative SBP operator and $\beta = -\frac{1}{2}$, $\sigma = \frac{1}{2}$, and $\tau \le -\frac{1}{2h\alpha_1}$ hold.*

Proof Let $\beta = -\frac{1}{2}$, $\sigma = \frac{1}{2}$. Multiplying Eq. 24 by $(\gamma v^{(l)})_t^T \bar{H}$ and $(\gamma v_t^{(r)})^T \bar{H}$, respectively, and adding the transpose leads to

$$
\frac{d}{dt}\left(\bar{E}_O^{(l)} + \bar{E}^{(r)} - z^T (R \otimes H) z \right) = 2\gamma (e_{Top}^T v_t^{(l)})^T H w_t \, ,
$$

11

where

$$\bar{E}_{\mathrm{O}}^{(l)} = \epsilon\gamma \|v_t^{(l)}\|_{\tilde{H}}^2 + \gamma(v^{(l)})^T \tilde{M} \otimes H v^{(l)} + \gamma(v^{(l)})^T H \otimes M v^{(l)} ,$$

$$\bar{E}^{(r)} = \epsilon\gamma \|v_t^{(r)}\|_{\tilde{H}}^2 + \gamma(v^{(r)})^T \tilde{M} \otimes H v^{(r)} + \gamma(v^{(r)})^T H \otimes M v^{(r)}$$
$$+ (\gamma e_{Top}^T v_t^{(r)})^T H (\gamma e_{Top}^T v_t^{(r)}) .$$

$\bar{E}_{\mathrm{O}}^{(l)}$ is a discrete analogue of the continuous energy given by (10), where $\gamma(v^{(l)})^T \tilde{M} \otimes H v^{(l)} + \gamma(v^{(l)})^T H \otimes M v^{(l)}$ mimics $\|\phi_x^{(l)}\|_\gamma^2 + \|\phi_y^{(l)}\|_\gamma^2$. The discrete energy in the right domain $\bar{E}^{(r)}$ mimics the corresponding continuous energy given by (14), since $\gamma(v^{(r)})^T \tilde{M} \otimes H v^{(r)} + \gamma(v^{(r)})^T H \otimes M v^{(r)}$ is a discrete analogue to $\|\phi_x^{(r)}\|_\gamma^2 + \|\phi_y^{(r)}\|_\gamma^2$. The term $z^T (R \otimes H) z$ is a correction from the interface coupling given by,

$$z = \begin{bmatrix} e_{East} v^{(l)} \\ e_{West} v^{(r)} \\ d_{1;East} v^{(l)} \\ d_{1;West} v^{(r)} \end{bmatrix} , \quad R = \begin{bmatrix} \tau & -\tau & \frac{1}{2} & -\frac{1}{2} \\ -\tau & \tau & \frac{1}{2} & -\frac{1}{2} \\ \frac{1}{2} & \frac{1}{2} & -h\,\alpha_1 & 0 \\ -\frac{1}{2} & -\frac{1}{2} & 0 & -h\,\alpha_1 \end{bmatrix} .$$

Here we have used Lemma 3.4 and the fact that D_2 is a narrow-diagonal SBP operator. By choosing $\tau \le -\frac{1}{2\,h\,\alpha_1}$, R is negative semi-definite and $\bar{E}_{\mathrm{O}}^{(l)} + \bar{E}^{(r)} - z^T (R \otimes H) z$ defines a semi-norm, and we obtain the following discrete energy estimate

$$\frac{d}{dt} \left(\bar{E}_{\mathrm{O}}^{(l)} + \bar{E}^{(r)} - z^T (R \otimes H) z \right) = 2\gamma e_{Top}^T v_t^{(l)})^T H w_t .$$

□

4.3. Stability analysis of the fully coupled problem

We will now utilise the stability analysis of the previous (uncoupled) problems and analyse stability of the fully coupled problem, given by (21) and (24). The energy estimate for the combined system is given by

$$\frac{d}{dt} \left(\bar{E}_{\mathrm{O}}^{(l)} + \bar{E}^{(r)} - z^T (R \otimes H) z + \bar{E}_{\mathrm{B}} + b\,\tilde{w}_1^T A_1 \tilde{w}_1 \right) = 0 , \tag{25}$$

where we have utilised the fact that $\gamma w_t^T H e_{Top}^T v_t^{(l)} = \gamma(e_{Top}^T v_t^{(l)})^T H w_t$. Hence, (25) exactly mimics the continuous energy estimate given by (15).

5. Time integration

The stability analysis in the previous section was done for the semi-discrete problem. Due to the nature of the problem, we expect the semi-discrete problem to be stiff. It is of course possible to time-integrate using an explicit method, such as the classical 4th order Runge-Kutta method, but numerical tests (not shown here) indicate the necessity of an implicit method for computational efficiency. In the present study we will distinguish between two different implicit time-integrators: 1.) an 8th order SBP-in-time discretisation (see [7] for details), and 2.) a second order centered finite difference approximation. To simplify the analysis we recast the semi-discrete problem, given by (21) and (24), into a second order ODE system given by

$$\begin{aligned} A q_{tt} &= -Bq - C q_t + G(t) , & t \ge 0 , \\ q &= f_1 , q_t = f_2 , & t = 0 , \end{aligned} \tag{26}$$

where f_1 and f_2 are initial data,

$$q^T = \begin{bmatrix} w & v^{(l)} & v^{(r)} \end{bmatrix} \ ,$$

$$A = \begin{bmatrix} a\,I_{m_x} & 0 & 0 \\ 0 & \epsilon\,I_{m_x} \otimes I_{m_y} & 0 \\ 0 & 0 & \epsilon\,I_{m_x} \otimes I_{m_y} + \gamma H_y^{-1} e_{North}^T e_{North} \end{bmatrix} \ ,$$

$$-B = \begin{bmatrix} B_{11} & 0 & 0 \\ 0 & B_{22} & B_{23} \\ 0 & B_{32} & B_{33} \end{bmatrix} \ .$$

$$-C = \begin{bmatrix} 0 & -\gamma e_{North}^T & 0 \\ H_y^{-1} e_{North} & 0 & 0 \\ 0 & 0 & 0 \end{bmatrix} \ ,$$

$$G(t) = \begin{bmatrix} 0 \\ 0 \\ H_x^{-1} e_{East} \bar{g}(t)) \end{bmatrix} \ ,$$

and

$$
\begin{aligned}
B_{11} = {}& -b\,D_4 - I_m + b\,H^{-1}(d_{3;1} - \tau_1 e_1^T)^T e_1^T - b\,H^{-1}(d_{2;1} + \tau_2 d_{1;1})^T d_{1;1} \\
& - \sigma_1 H^{-1} d_{1;m}^T d_{2;m} + \sigma_2 H^{-1} e_m d_{3;m} \\
B_{22} = {}& D_{2x} + D_{2y} + \tau H_x^{-1} e_{East} e_{East}^T + \sigma H_x^{-1} d_{1;East}^T e_{East}^T + \gamma H_x^{-1} e_{East} d_{1;East} \\
& + H_x^{-1} e_{West} d_{1;West} + H_y^{-1} e_{South} d_{1;South} - H_y^{-1} e_{North} d_{1;North} \\
B_{33} = {}& D_{2x} + D_{2y} + \tau H_x^{-1} e_{West} e_{West}^T - \sigma H_x^{-1} d_{1;West}^T e_{West}^T - \gamma H_x^{-1} e_{West} d_{1;West} \\
& - H_x^{-1} e_{East} d_{1;East} + H_y^{-1} e_{South} d_{1;South} - H_y^{-1} e_{North} d_{1;North} \\
B_{23} = {}& -\tau H_x^{-1} e_{East} e_{West}^T - \sigma H_x^{-1} d_{1;East}^T e_{West}^T - \gamma H_x^{-1} e_{East} d_{1;West} \ , \\
B_{32} = {}& -\tau H_x^{-1} e_{West} e_{East}^T + \sigma H_x^{-1} d_{1;West}^T e_{East}^T + \gamma H_x^{-1} e_{West} d_{1;East} \ .
\end{aligned}
$$

Here

$$\tau_1 \geq \frac{2}{h^3 \alpha_3}, \ \tau_2 \geq \frac{2}{h \alpha_2}, \ \sigma_1 = \sigma_2 = -b, \ \tau \leq -\frac{1}{2\,h \alpha_1}, \ \gamma = -\frac{1}{2}, \ \sigma = \frac{1}{2} \ .$$

The values of the parameter α_1 (for different orders of accuracy) are presented in Table 1 and the values of $\alpha_{2,\,3}$ are presented in Table 2.

A, B, and C are $m_3 \times m_3$ matrices, where $m_3 = m_x^2 \times m_y$. We introduce $\tilde{A} = \bar{H}_3 A$, $\tilde{B} = \bar{H}_3 B$, $\tilde{C} = \bar{H}_3 C$ where $\bar{H}_3$ is given by

$$\bar{H}_3 = \begin{bmatrix} H & 0 & 0 \\ 0 & \gamma \bar{H} & 0 \\ 0 & 0 & \gamma \bar{H} \end{bmatrix} \ . \tag{27}$$

Definition 5.1. *If $\tilde{A} = \tilde{A}^T$ is positive definite and $\tilde{B} = \tilde{B}^T$ is positive semi-definite,*

$$E_H = q_t^T \tilde{A} q_t + q^T \tilde{B} q \ ,$$

is non-negative and $E_H = 0$ implies that $q_t = 0$. Hence, E_H defines a semi-norm.

Lemma 5.2. *If $\tilde{A} = \tilde{A}^T \geq 0$, $\tilde{C} + \tilde{C}^T \geq 0$ and $\tilde{B} = \tilde{B}^T \geq 0$, the ODE system (26) is stable.*

13

Proof Multiplying the homogeneous version of (26) by $q_t^T \bar{H}_3$ and adding the transpose leads to

$$q_t^T \bar{H}_3 A q_{tt} + q_{tt}^T (\bar{H}_3 A)^T q_t = -q_t^T (\bar{H}_3 B) q - q^T (\bar{H}_3 B)^T q_t - q_t^T (\bar{H}_3 C - (\bar{H}_3 C)^T) q_t$$

$$\Downarrow$$

$$\frac{d}{dt} E_H = -q_t^T (\tilde{C} + \tilde{C}^T) q_t \ .$$

In the last step we use the fact that $\tilde{A} = \tilde{A}^T$ is positive definite and $\tilde{B} = \tilde{B}^T$ is positive semi-definite such that E_H defines a semi-norm (see Definition 5.1). If $\tilde{C} + \tilde{C}^T \geq 0$ the time-growth of E_H is non-positive. $\square$

The semi-discrete SBP-SAT approximation of the fully coupled problem, given by (21) and (24), fulfils (26) such that the conditions in Lemma 5.2 hold.

5.1. 8th order SBP in time

In [47, 33] a novel idea to discretise a first order ODE system using SBP operators was presented. In the present study we will utilize an 8th order accurate SBP discretisation presented in [7]. The SBP discretisation is very accurate, but requires the ODE system (26) to be recast into first order form and is also rather memory consuming. An alternative implicit method is presented in the next subsection.

5.2. 2nd order implicit in time

Here we will present an implicit, second order accurate finite difference method that does not require reformulation into first order form. For many applications with only modest accuracy requirements, this method is likely to be the most efficient.

Let $t_n = n\,k$, $n = 0, 1, \ldots$ denote the discrete time-levels, where k is the time-step, and introduce the notation $q^n = q(t_n)$. We introduce the following second-order accurate central finite difference approximations, $D_0 q^n = (q^{n+1} - q^{n-1})/(2\,k)$ and $D_+ D_- q^n = (q^{n+1} - 2q^n + q^{n-1})/k^2$, of the first and second derivatives in (26). The first derivative in the initial step can be approximated with $D_+ q^0 = (q^1 - q^0)/k$. By replacing the first derivative in the initial step by $D_+ q^0$ and inserting appropriate Taylor expansions we obtain the following second-order accurate approximation of (26):

$$A\frac{q^{n+1} - 2q^n + q^{n-1}}{k^2} = -B\frac{q^{n+1} + q^{n-1}}{2} - C\frac{q^{n+1} - q^{n-1}}{2\,k} + G^n \ , n = 1, \ldots$$
$$q^0 = f_1, \ \frac{q^1 - f_1}{k} = f_2 - \frac{k}{2} A^{-1}(Bf_1 + Cf_2 - G^0) \ . \tag{28}$$

Definition 5.3. *Let $\bar{A} = \bar{A}^T$ and $\bar{B} = \bar{B}^T$. If $\bar{A}$ is positive definite and $\bar{B}$ is positive semi-definite,*

$$E^n = \left(D_+ q^n, \bar{A} D_+ q^n\right) + \left(\frac{q^{n+1} + q^n}{2}, \bar{B}\frac{q^{n+1} + q^n}{2}\right) \ ,$$

is non-negative for all q^n, q^{n+1} and $E^n = 0$ imply $q^{n+1} = q^n$. Hence, E^n defines a semi-norm. Here we define $\left(D_+ q^n, \bar{A} D_+ q^n\right) = (D_+ q^n)^T \bar{A} (D_+ q^n)$.

We will make use of the following two relations (where $\bar{A} = \bar{A}^T$ and $\bar{B} = \bar{B}^T$):

$$\left(q^{n+1} - q^{n-1}, \bar{A}(q^{n+1} + q^{n-1})\right) + \left(q^{n+1} + q^{n-1}, \bar{A}(q^{n+1} - q^{n-1})\right)$$
$$= 2\left(q^{n+1} - q^n, \bar{A}(q^{n+1} - q^n)\right) + 4\left(q^{n+1}, \bar{A}q^n\right) \tag{29}$$
$$- 2\left(q^n - q^{n-1}, \bar{A}(q^n - q^{n-1})\right) - 4\left(q^n, \bar{A}q^{n-1}\right) \ ,$$

$$\left(q^{n+1}, \bar{B}q^n\right) + \left(q^n, \bar{B}q^{n+1}\right) = \frac{1}{2}\left(q^{n+1} + q^n, \bar{B}(q^{n+1} + q^n)\right)$$
$$- \frac{1}{2}\left(q^{n+1} - q^n, \bar{B}(q^{n+1} - q^n)\right) \ . \tag{30}$$

The following Theorem is one of the main results in the present study:

Theorem 5.4. *Eq. 28 is an unconditionally stable approximation of (26) if Lemma 5.2 applies.*

Proof Start by setting $G = 0$ (since G does not affect stability), and rewrite (28) as

$$\left(\frac{A}{k^2} + \frac{B}{2}\right)\frac{q^{n+1} + q^{n-1}}{k^2} = \left(2\frac{A}{k^2}\right)q^n - C\frac{q^{n+1} - q^{n-1}}{2\,k} \ .$$

Multiplying by $\left(\frac{q^{n+1} - q^{n-1}}{2\,k}\right)^T \bar{H}_3$ leads to

$$\left(\frac{q^{n+1} - q^{n-1}}{2\,k}, \left(\frac{\tilde{A}}{k^2} + \frac{\tilde{B}}{2}\right)\left(\frac{q^{n+1} + q^{n-1}}{k^2}\right)\right) =$$
$$-\left(\frac{q^{n+1} - q^{n-1}}{2\,k}, \left(2\frac{\tilde{A}}{k^2}\right)v^n\right) - \left(\frac{q^{n+1} - q^{n-1}}{2\,k}, \tilde{C}\left(\frac{q^{n+1} - q^{n-1}}{2\,k}\right)\right) \ .$$

By adding the transpose, assuming $\tilde{A} = \tilde{A}^T$ and $\tilde{B} = \tilde{B}^T$, we obtain

$$\left(\frac{q^{n+1} - q^{n-1}}{2\,k}, \left(\frac{\tilde{A}}{k^2} + \frac{\tilde{B}}{2}\right)\left(\frac{q^{n+1} + q^{n-1}}{k^2}\right)\right) +$$
$$\left(\frac{q^{n+1} + q^{n-1}}{k^2}, \left(\frac{\tilde{A}}{k^2} + \frac{\tilde{B}}{2}\right)^T\left(\frac{q^{n+1} - q^{n-1}}{2\,k}\right)\right)$$
$$= -\left(\frac{q^{n+1} - q^{n-1}}{2\,k}, \left(2\frac{\tilde{A}}{k^2}\right)v^n\right) - \left(q^n, \left(2\frac{\tilde{A}}{k^2}\right)^T\frac{q^{n+1} - q^{n-1}}{2\,k}\right)$$
$$- \left(\frac{q^{n+1} - q^{n-1}}{2\,k}, (\tilde{C} + \tilde{C}^T)\left(\frac{q^{n+1} - q^{n-1}}{2\,k}\right)\right) \ .$$

By using the two relations (29) and (30) we obtain

$$\frac{1}{k}\left(D_+q^n, \left(\tilde{A} + \frac{k^2}{4}\tilde{B}\right)D_+q^n\right) + \frac{1}{k}\left(\frac{q^{n+1} + q^n}{2}, \frac{1}{4}\tilde{B}\frac{q^{n+1} + q^n}{2}\right) =$$
$$\frac{1}{k}\left(D_+q^{n-1}, \left(\tilde{A} + \frac{k^2}{4}\tilde{B}\right)D_+q^{n-1}\right) + \frac{1}{k}\left(\frac{q^{n-1} + q^n}{2}, \frac{1}{4}\tilde{B}\frac{q^{n-1} + q^n}{2}\right)$$
$$- \left(D_0q^n, (\tilde{C} + \tilde{C}^T)D_0q^n\right) \ .$$

This can be written as

$$\frac{E^{n+1} - E^n}{k} = -\left(D_0q^n, (\tilde{C} + \tilde{C}^T)D_0q^n\right) \ ,$$

where the semi-norm E^n is given by Definition 5.3, where $\bar{A} = \tilde{A} + \frac{k^2}{4}\tilde{B}$ is positive definite and $\bar{A} = \frac{1}{4}\tilde{B}$ is positive semi-definite . If $\tilde{C} + \tilde{C}^T \geq 0$ we conclude that the time-growth of the semi-norm E^n is bounded.
$\square$

6. Numerical verifications

In this section the accuracy and convergence properties of the SBP-SAT approximations, defined by (21) and (24), are verified by numerical simulations. We perform three verification tests: 1.) waves in the fully ice-covered domain, as defined in Section 2.1; 2.) waves in the open ocean domain, as defined in Section 2.2;

and 3.) waves in the fully coupled problem (left and right domain coupled). For all computations the 8th order (SBP) implicit time integrator is employed, to make sure the time discretisation errors are negligible.

The first two verification tests employ analytical plane-wave solutions for the time-harmonic problem. Inhomogeneous BC are set so that the surface plane waves for the respective problems are exact solutions. In Figure 3 we present the initial conditions of ϕ and w for the two different cases.

(a) Ice covered domain (first test)   (b) Open water domain (second test)
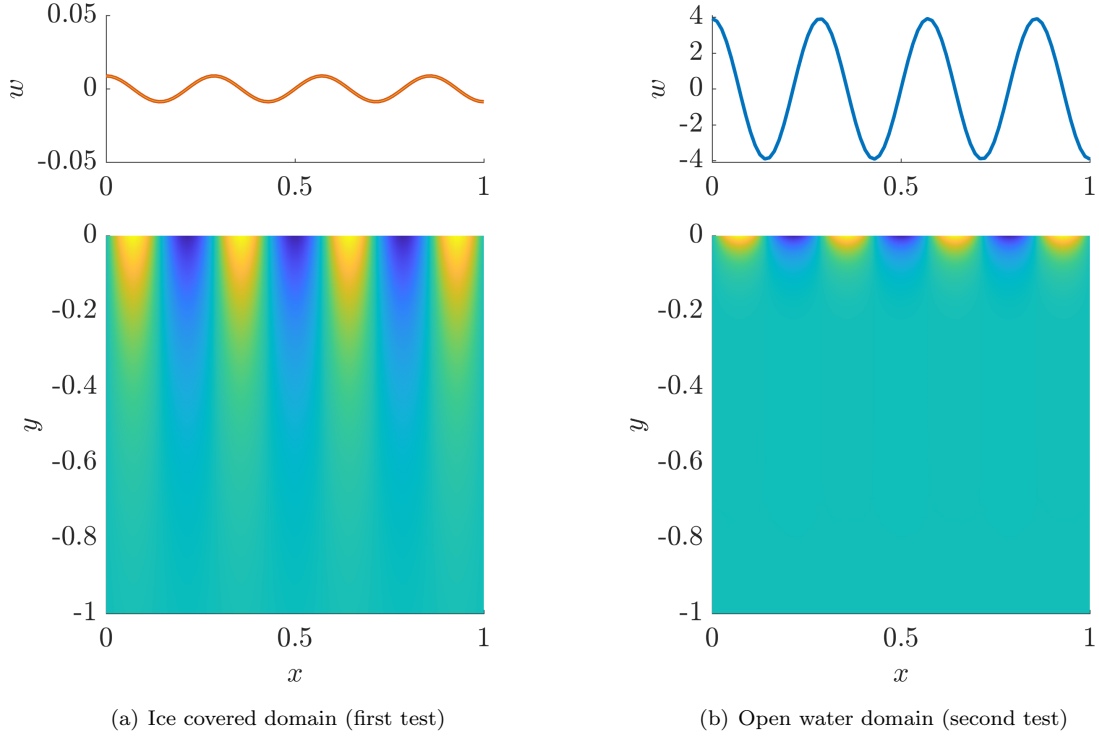
Figure 3: Initial conditions (ϕ and w) for the first and second verification test problems involving time-harmonic wave solutions. The wave disturbance is confined to the surface, especially for the open water test.

For the fully coupled problem (the third verification test), an analytic solution cannot easily be derived without the inclusion of mathematical forcing functions. An alternative, chosen here, is to replace the analytic solution with a computation done on a very fine grid, i.e., comparing against an accurate reference solution. The parameter values used for all three verification tests are presented in Table 3.

Verification/parameters	a	b	γ	ϵ
Ice covered (test 1)	0.18	0.32	0.7	2.2e-3
Open water (test 2)			0.7	2.2e-3
Fully coupled (test 3)	0.1112	1.2419	0.4916	2.6e-3

Table 3: Parameter values used for the three verification tests.

6.1. Test 1: Ice-covered domain

An analytic solution to (1) and (2), in infinite depth water, is given by

$$
\phi = e^{\lambda y} \sin(\kappa x - \omega t),
$$
$$
w = \frac{\lambda}{\omega} \cos(\kappa x - \omega t),
$$

(31)

where

$$\lambda = \frac{\omega^2 \gamma}{-a\omega^2 + b\kappa^4 + 1}, \tag{32}$$

and κ and ω satisfy the dispersion relation

$$(-a\omega^2 + b\kappa^4 + 1)^2 \kappa^2 = \epsilon \omega^2 + \omega^4 \gamma^2. \tag{33}$$

This is a third order polynomial in ω^2 which can easily be solved numerically (or using a symbolic math software). In the numerical simulations we set $k = 7\pi$ which leads to $\omega \approx 461$ and $\lambda \approx 4$. The initial data is presented in Figure 3. The solution is evolved for 3 periods, i.e., until time $T = 3 \times 2\pi/\omega$. The time step was set to $(2\pi/\omega)/5$ for the coarsest grid and then refined together with the grid resolution (,i.e., if N is doubled the time step is reduced by a factor of 2.) The convergence results for the $2nd$, $4th$ and $6th$ order accurate SBP-SAT approximations are shown in Table 4 and Figure 4. The discrete l_2-errors are computed for the full wave field, including both ϕ and w. Here q denotes the convergence rate.

N	2th order		4th order		6th order	
	$\log_{10}(l_2)$	q	$\log_{10}(l_2)$	q	$\log_{10}(l_2)$	q
31	-0.26		-1.11		-1.43	
43	-0.54	-1.91	-1.80	-4.74	-2.32	-6.13
61	-0.86	-2.04	-2.47	-4.30	-3.37	-6.76
86	-1.17	-2.05	-3.10	-4.18	-4.39	-6.74
121	-1.47	-2.03	-3.73	-4.20	-5.35	-6.40

Table 4: Convergence results for the ice-covered problem, comparing the $2nd$, $4th$ and $6th$ order approximations. N is the number of grid points in the x-direction.

(a) Ice covered domain (first test)
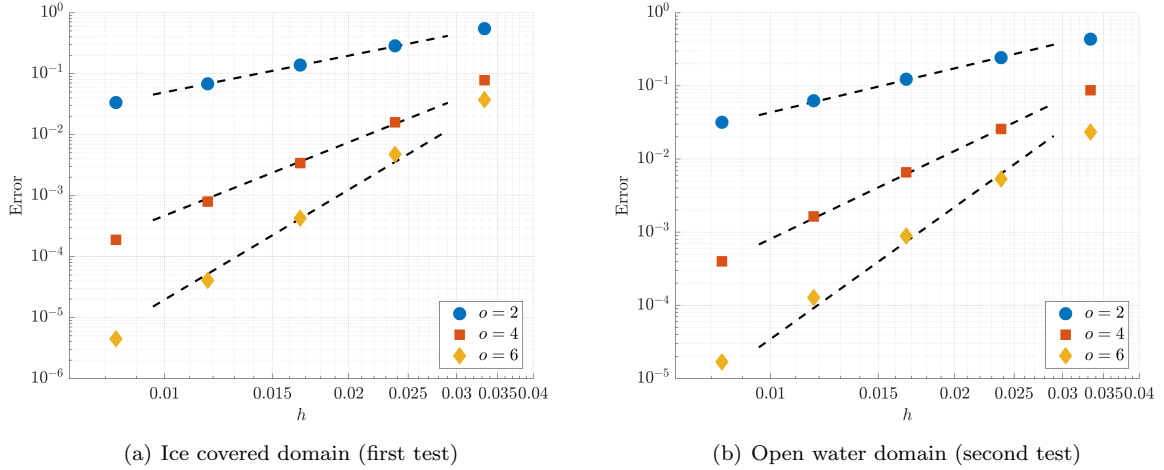
(b) Open water domain (second test)

Figure 4: Convergence results (in the left and right subfigures) are taken from Tables 4 and 5.

6.2. Test 2: Open-water domain

An analytic solution to (6), in infinite depth water, for the open water domain is given by

$$\phi = e^{\lambda y} \sin(\kappa x - \omega t), \tag{34}$$

where $\lambda = \gamma \omega^2$, while κ and ω satisfy

$$-\gamma^2 \omega^4 + \epsilon \omega^2 - \kappa^2 = 0. \tag{35}$$

17

Solving for ω^2 we have

$$\omega^2 = -\frac{\epsilon}{2\gamma^2} + \sqrt{\frac{\epsilon^2}{4\gamma^4} + \frac{\kappa^2}{\gamma^2}}. \tag{36}$$

In the numerical simulations we set $k = 7\pi$ which leads to $\omega \approx 5.6$ and $\lambda \approx 22$. The solution is evolved for 3 wave periods, i.e., until $T = 3 \times 2\pi/\omega$. The time step was set to $(2\pi/\omega)/5$ for the coarsest grid and then refined together with the grid resolution. The convergence results for the $2nd$, $4th$ and $6th$ order accurate SBP-SAT approximations are shown in Table 5 and Figure 4.

	2th order		4th order		6th order	
N	$\log_{10}(l_2)$	q	$\log_{10}(l_2)$	q	$\log_{10}(l_2)$	q
31	-0.36		-1.06		-1.63	
43	-0.62	-1.75	-1.59	-3.61	-2.28	-4.41
61	-0.91	-1.89	-2.18	-3.83	-3.05	-5.02
86	-1.20	-1.95	-2.79	-3.99	-3.90	-5.57
121	-1.50	-1.98	-3.40	-4.09	-4.78	-5.88

Table 5: Convergence results for the open ocean problem, comparing the $2nd$, $4th$ and $6th$ order approximations. N is the number of grid points in the x-direction.

6.3. Test 3: Fully coupled problem

To achieve a realistic setup for the fully coupled problem we use a domain of length $L = 15.73$ and water depth $D = 0.4916$, where the left half is covered with ice and the right half has no ice cover. The side and bottom water boundaries have homogeneous Neumann (no flow) boundary conditions. The parameters a, b, γ, and ϵ (Table 3) are representative of a thick ice shelf. The initial condition is set to a Gaussian-shaped pulse in the velocity potential of the water,

$$\phi = \exp(-\frac{1}{2}(x - \frac{3}{4}L)^2/D^2), \tag{37}$$

with $\phi_t = 0$. The ice starts in an undeformed rest state, $w = w_t = 0$, and is clamped, $w = w_x = 0$, at the left boundary and free, $w_{xx} = w_{xxx} = 0$, at the right boundary.

The problem is solved to final time $T = 62.92$ on a series of grids using the prescribed method and the 8th order time-integration scheme. The time step is chosen as $T/16$ for the coarsest grid and is then refined together with the spatial dimension. The reference solution (see Figure 6) was obtained using 2177×18 grid points computed with the $6th$ order accurate discretisation. The convergence results for the $2nd$, $4th$ and $6th$ order accurate SBP-SAT approximations are shown in Table 6 and Figure 5.

Remark We suspect that the somewhat irregular convergence behavior is attributed to the discontinuity in the solution that develops at the ice edge, which arises from the change in top surface boundary condition for the water PDE. Despite this discontinuity, the convergence test demonstrates that the high-order methods are superior to the second-order method on fine meshes.

	2th order		4th order		6th order	
N	$log_{10}(l_2)$	q	$log_{10}(l_2)$	q	$log_{10}(l_2)$	q
69	-0.25		-0.23		-0.23	
137	-0.68	-1.43	-0.75	-1.74	-0.75	-1.74
273	-1.58	-3.00	-1.80	-3.47	-1.80	-3.48
545	-1.91	-1.10	-3.59	-5.94	-3.75	-6.48

Table 6: Convergence results for the fully coupled problem, comparing the $2nd$, $4th$ and $6th$ order approximations. N is the number of grid points in the x-direction.
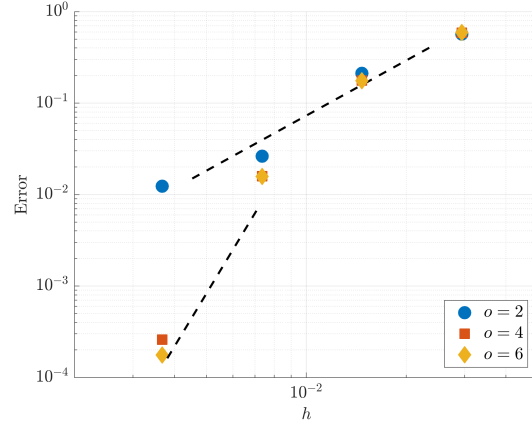
Figure 5: Convergence for the coupled problem. The dashed lines show convergence rates 2 and 6. Results are from Table 6.
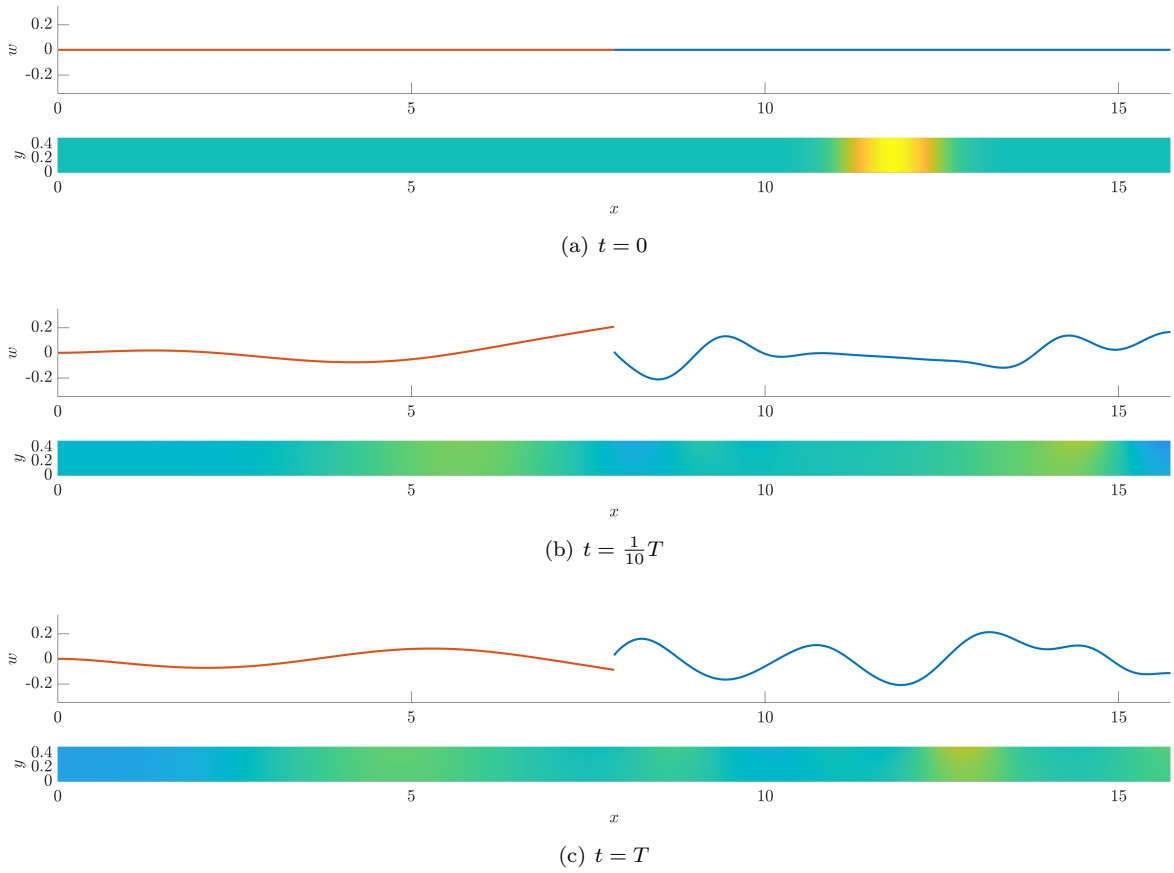
6.

(a) $t = 0$

(b) $t = \frac{1}{10}T$

(c) $t = T$

Figure 6: Reference solution (w and ϕ) to the fully coupled problem at three different times, obtained using the 6th order space discretisation and 2177×18 grid-points. $T = 62.92$.

19

parameter	value	units
water depth, H	600	m
water density, ρ_w	1000	kg/m^3
water sound speed, c_w	1500	m/s
gravitational acceleration, g	9.8	m/s^2
ice density, ρ_i	920	kg/m^3
ice thickness, h	100, 200, 300	m
ice bending stiffness, D	$10^{15} \times (h/100 \text{ m})^3$	N m

Table 7: Parameters for the study of reflection/transmission and flexural-gravity wave dispersion.

7. Applications

In this section we demonstrate how our newly developed code can be used to study the interaction of incident ocean waves with ice shelves. We revert to dimensional parameters, using the notation in Appendix A, and select water depths, ice thicknesses, and other parameters (Table 7) to approximately coincide with ice shelves in Antarctica. Results of the study are summarized in Figure 7.

As in Figure 1, the domain is divided into an open-water region ($0 < x < 50$ km) and an ice-covered region (-50 km $< x < 0$). Uniform grid spacings of 50 m and 30 m are used in the horizontal and vertical directions, respectively, and the solution is evolved using the second-order time stepping method of Section 5.2 with a constant time step of 1 s. Waves are initialized in the open water using a nonzero initial pressure distribution, which is depth-independent and of Gaussian shape in the horizontal direction (having standard deviation, or width, equal to the water depth H and centered at $x = 10$ km). Surface gravity waves in the open ocean span a range of wavelengths or periods, with the longest periods propagating in the shallow water limit with speed $(gH)^{1/2}$ and shorter periods propagating more slowly. Upon encountering the ice edge, the waves are both reflected back into the open water and transmitted into the ice-covered water. Transmission is favored for thinner ice and at longer periods. Upon entering the ice-covered region, the waves become anamolously dispersed flexural-gravity waves that reflect from the grounding line (i.e., clamped boundary) at $x = -50$ km.

8. Conclusions and future work

We developed a provably stable high-order accurate SBP-SAT finite difference method for flexural-gravity waves and other waves in a compressible ocean partially covered in ice. To guarantee stability we employ SBP operators (derived in [41, 42]) to approximate the fourth-derivative term in the dynamic beam equation, and the second derivative terms in the wave equation for velocity potential, combined with the SAT technique to impose the BC and interface conditions weakly. Numerical computations corroborate the stability and accuracy properties and show that the higher-order accurate approximations are superior to the corresponding second-order accurate SBP-SAT schemes.

While the example simulations in this study are limited to relatively simple geometries and problems, slight generalizations of the method can be used to study more complex problems. For example, by adding additional water blocks, with appropriate coupling between them, we could account for thinner water beneath the ice shelf than external to it. The ice-shelf/ocean model we have developed could also be coupled to an underlying elastic half-space, obeying the elastic wave equation, to study how seismic surface waves are influenced by the ocean and ice layers. Such studies are essential to properly interpret the wealth of new observations that are being made on ice shelves.
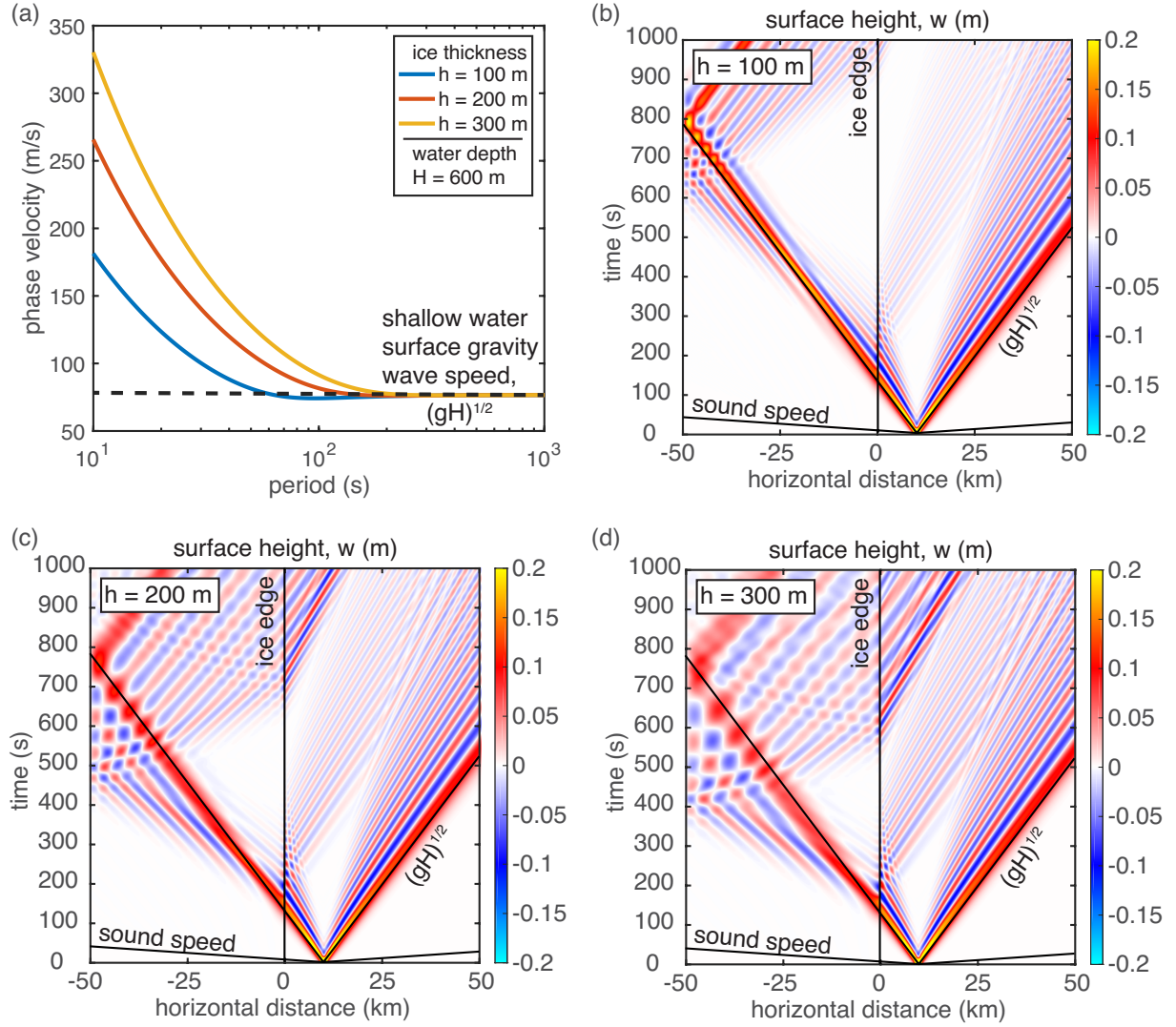
9. Acknowledgements

Figure 7: (a) Flexural-gravity wave dispersion curves for different ice thicknesses h (with other parameters given in Table 7). (b)-(d) Space-time plots of surface uplift $w(x,t)$ illustrating reflection/transmission of surface gravity waves from open-water region ($x > 0$) to ice shelf ($x < 0$). Thicker ice increases phase velocity, leading to more pronounced dispersion (with shorter wavelengths and periods propagating faster in the ice). Black lines show shallow wave wave speed in open water, $(gH)^{1/2}$, and sound speed.

Appendix A. Governing equations and nondimensionalization

In this section we introduce the governing equations of the water and ice. We nondimensionalize the equations using scalings relevant to FGWs and discuss the meaning of the dimensionless parameters.

Consider a body of water of uniform depth H, density ρ_w, and sound speed c_w. Let x and y be horizontal and vertical coordinates, with y positive up and $y = 0$ the location of the equilibrium water surface. Neglecting stratification and assuming spatially uniform properties, the velocity potential $\phi(x, y, t)$ obeys the wave equation (e.g., [29, 62])

$$-c_w^{-2}\phi_{tt} + \phi_{xx} + \phi_{yy} = 0, \tag{A.1}$$

with horizontal and vertical particle velocities given by

$$u = \phi_x \quad \text{and} \quad v = \phi_y \tag{A.2}$$

and pressure by

$$p = -\rho_w \phi_t. \tag{A.3}$$

Thus ϕ, u, v, and p all depend on x, y, t, while ρ_w and c_w are constant.

The perturbed surface of the water is $y = w(x, t)$. Assuming small amplitude waves, the problem is linearized so that boundary conditions can be applied on the unperturbed surface $y = 0$. The linearized kinematic condition is

$$w_t = v(x, 0, t) = \phi_y(x, 0, t), \tag{A.4}$$

using (A.2) for the last equality.

The water surface boundary condition involves pressure on the moving water surface, $p(x, w(x, t), t)$. In the context of our linearized theory and accounting for gravity, this pressure is given by [28, 32]

$$p(x, w(x, t), t) \approx p(x, 0, t) - \rho_w g w(x, t) = -\rho_w \left[\phi_t(x, 0, t) + gw(x, t)\right], \tag{A.5}$$

where g is the gravitational acceleration, and the last equality follows from (A.3). The $-\rho_w g w$ term accounts for the hydrostatic increase of pressure with depth in the unperturbed reference state, and vanishes in the absence of gravity ($g = 0$).

In open water (i.e., no ice shelf), pressure on the surface is set equal to zero: $p(x, w(x, t), t) = 0$ or, using (A.5),

$$\phi_t(x, 0, t) + gw(x, t) = 0. \tag{A.6}$$

For this open water case, equations (A.4) and (A.6) can be combined, by taking $\partial/\partial t$ of (A.6) and using (A.4) to eliminate w_t, into a single condition on ϕ:

$$\phi_{tt}(x, 0, t) + g\phi_y(x, t) = 0. \tag{A.7}$$

With an ice layer, the pressure in (A.5) is set equal to the vertical elastic restoring force per unit area from ice flexure, $q(x, t)$:

$$-\rho_w \left[\phi_t(x, 0, t) + gw(x, t)\right] = q(x, t). \tag{A.8}$$

The ice obeys the Euler-Bernoulli plate equation, describing an elastic plate subject to load q:

$$\rho_i h w_{tt} + D w_{xxxx} = q(x, t), \tag{A.9}$$

22

where ρ_i is the ice density, h is the ice thickness, and D is the bending stiffness, all assumed to be spatially uniform. Equations (A.8) and (A.9) can be combined into a single equation by eliminating q:

$$\rho_i h w_{tt} + D w_{xxxx} = -\rho_w \left[\phi_t(x,0,t) + g w(x,t)\right], \tag{A.10}$$

which must be solved together with the kinematic condition (A.4).

There are many ways to nondimensionalize these equations. We do this using a scaling appropriate for shallow water surface gravity waves. In open water, such waves (having wavelength much greater than the water depth H) propagate without dispersion at speed $\sqrt{gH}$. Let ω be a characteristic angular frequency and $\omega/\sqrt{gH}$ be the associated characteristic wavenumber. Time and distance are nondimensionalized as $t' = \omega t$, $x' = \omega x/\sqrt{gH}$, and $y' = \omega y/\sqrt{gH}$, where nondimensional variables are denoted with a prime. Let A be the characteristic wave amplitude, such that $w' = w/A$. In addition, $p' = p/(\rho_w g A)$ and $\phi' = \phi/(\sqrt{gH}A)$. With these definitions, the governing equations and boundary conditions can be nondimensionalized.

We now drop the primes and present the nondimensional equations and dimensionless parameters. Equation (A.1) becomes

$$-\epsilon \phi_{tt} + \phi_{xx} + \phi_{yy} = 0, \tag{A.11}$$

where

$$\epsilon \equiv gH/c_w^2. \tag{A.12}$$

In Earth's oceans, $\epsilon \ll 1$, and the smallness of this parameter justifies the relative unimportance of compressibility on surface gravity waves and gravity on acoustic waves [57, 19]. The open water condition (A.7) becomes

$$\gamma \phi_{tt}(x,0,t) + \phi_y(x,0,t) = 0, \tag{A.13}$$

where

$$\gamma \equiv \omega\sqrt{H/g}. \tag{A.14}$$

In ice-covered water, the kinematic condition (A.4) is

$$w_t = \phi_y(x,0,t) \tag{A.15}$$

and the plate equation is

$$a w_{tt} + b w_{xxxx} = -\gamma \phi_t(x,0,t) - w(x,t), \tag{A.16}$$

where

$$a \equiv \frac{\rho_i h \omega^2}{\rho_w g} \quad \text{and} \quad b \equiv \frac{D\omega^4}{\rho_w g^3 H^2} = \left[\frac{\omega}{\sqrt{gH}}\left(\frac{D}{\rho_w g}\right)^{1/4}\right]^4. \tag{A.17}$$

The parameter a quantifies the importance of inertia of the ice (i.e., the additional mass of the ice layer) and b quantifies ice rigidity (i.e., flexural restoring forces and elastic resistance to bending). The second form of b reveals the product of the characteristic wavenumber of shallow water waves, $\omega/\sqrt{gH}$, and the flexural length, $(D/\rho_w g)^{1/4}$. Parameter estimates for Antarctic ice shelves demonstrate that a, b, and γ are $O(0.1-1)$ at relevant wave periods ~ 10 to 300 s.

Appendix B. SBP operators

Below we list the second-derivative SBP operators for the second-, fourth- and sixth-order cases (first reported in [41, 45]). The second-derivative operator

$$D_2^{(b)} = H^{-1}(-M^{(b)} + b_m e_m d_{1;m} - b_1 e_1 d_{1;1}),$$

approximates $\partial/\partial x\,(\,b(x)\,\partial/\partial x)$, where $b(x) > 0$. The fourth-derivative SBP operator is given by,

$$D_4 = H^{-1}\left(N - e_1 d_{3;1} + e_m d_{3;m} + d_{1;1}^T d_{2;1} - d_{1;m}^T d_{2;m}\right)\ .$$

The boundary closures (the coefficients) are presented for the H, $M^{(b)}$ and N matrices. Notice that the coefficients in H, $M^{(b)}$ and N should be multiplied by h, $\frac{1}{h}$ and $\frac{1}{h^3}$, respectively. Here h denotes the grid-spacing.

Appendix B.1. Second order case.

The boundary derivative operators are given by

$$d_{1;1}v = \tfrac{-3v_1 + 4v_2 - v_3}{2\,h}, \qquad d_{1;m}v = \tfrac{+3v_m - 4v_{m\ 1} + v_{m\ 2}}{6\,h}$$

$$d_{2;1}v = \tfrac{v_1 - 2v_2 + 1v_3}{h^2}, \qquad d_{2;m}v = \tfrac{v_m - 2v_{m\ 1} + v_{m\ 2}}{h^2}$$

$$d_{3;1}v = \tfrac{-v_1 + 3v_2 - 3v_3 + v_4}{h^3}, \quad d_{3;m}v = \tfrac{+v_m - 3v_{m\ 1} + 3v_{m\ 2} - v_{m\ 3}}{h^3}$$

The interior schemes of D_4 is given by

$$(D_4 v)_j = \frac{v_{j-2} - 4v_{j-1} + 6v_j - 4v_{j+1} + v_{j+2}}{h^4}$$

The norm is the traditional second order norm, i.e, the first and last coefficients are given by $H_{1,1} = H_{m,m} = \frac{1}{2}$, and the interior is a diagonal matrix with ones. Notice that the coefficients in the norm H should be multiplied by h to have the correct scaling with h.

The left boundary closure of $M^{(b)}$ (given by a 3×3 matrix) is given by

$$
\begin{bmatrix}
\tfrac{1}{2}\,b_1 + \tfrac{1}{2}\,b_2 & -\tfrac{1}{2}\,b_1 - \tfrac{1}{2}\,b_2 & 0 \\
-\tfrac{1}{2}\,b_1 - \tfrac{1}{2}\,b_2 & \tfrac{1}{2}\,b_1 + b_2 + \tfrac{1}{2}\,b_3 & -\tfrac{1}{2}\,b_2 - \tfrac{1}{2}\,b_3 \\
0 & -\tfrac{1}{2}\,b_2 - \tfrac{1}{2}\,b_3 & \tfrac{1}{2}\,b_2 + b_3 + \tfrac{1}{2}\,b_4
\end{bmatrix}.
$$

The corresponding right boundary closure is given by replacing $b_i \to b_{m+1-i}$ for $i = 1..4$ followed by a permutation of both rows and columns.

The interior stencil of $M^{(b)}$ at row i is given by ($i = 4 \ldots m - 3$):

$$m_{i,i-1} = -\tfrac{1}{2}\,b_{i-1} - \tfrac{1}{2}\,b_i$$

$$m_{i,i} \;\;= \tfrac{1}{2}\,b_{i-1} + b_i + \tfrac{1}{2}\,b_{i+1}$$

$$m_{i,i+1} = -\tfrac{1}{2}\,b_i - \tfrac{1}{2}\,b_{i+1}$$

The upper part of N,

$$N_{1,1} = \tfrac{13}{10} \qquad N_{1,3} = \tfrac{9}{10} \qquad N_{2,2} = \tfrac{26}{5} \qquad N_{2,4} = \tfrac{2}{5} \qquad N_{3,4} = -\tfrac{17}{5}$$

$$N_{1,2} = -\tfrac{12}{5} \qquad N_{1,4} = \tfrac{1}{5} \qquad N_{2,3} = -\tfrac{16}{5} \qquad N_{3,3} = \tfrac{47}{10} \qquad N_{4,4} = -\tfrac{29}{5}$$

Appendix B.2. Fourth order case.

The boundary derivative operators are given by

$$d_{1;1}v = \tfrac{-11v_1 + 18v_2 - 9v_3 + 2v_4}{6\,h}, \quad d_{1;m}v = \tfrac{+11v_m - 18v_{m\ 1} + 9v_{m\ 2} - 2v_{m\ 3}}{6\,h}$$

$$d_{2;1}v = \tfrac{2v_1 - 5v_2 + 4v_3 - v_4}{h^2}, \qquad d_{2;m}v = \tfrac{2v_m - 5v_{m\ 1} + 4v_{m\ 2} - 1v_{m\ 3}}{h^2}$$

$$d_{3;1}v = \tfrac{-v_1 + 3v_2 - 3v_3 + v_4}{h^3}, \qquad d_{3;m}v = \tfrac{+v_m - 3v_{m\ 1} + 3v_{m\ 2} - v_{m\ 3}}{h^3}$$

24

The interior scheme of D_4 is given by

$$(D_4 v)_j = \frac{-v_{j-3} + 12v_{j-2} - 39v_{j-1} + 56v_j - 39v_{j+1} + 12v_{j+2} - v_{j+3}}{6\,h^4}$$

The upper part of the norm H,

$$H_{1,1} = \tfrac{17}{48} \quad H_{2,2} = \tfrac{59}{48} \quad H_{3,3} = \tfrac{43}{48} \quad H_{4,4} = \tfrac{49}{48}$$

The interior stencil of $-M^{(b)}$ at row i is given by $(i = 7 \ldots m - 6)$:

$$m_{i,i-2} = \tfrac{1}{6} b_{i-1} - \tfrac{1}{8} b_{i-2} - \tfrac{1}{8} b_i$$
$$m_{i,i-1} = \tfrac{1}{6} b_{i-2} + \tfrac{1}{6} b_{i+1} + \tfrac{1}{2} b_{i-1} + \tfrac{1}{2} b_i$$
$$m_{i,i} = -\tfrac{1}{24} b_{i-2} - \tfrac{5}{6} b_{i-1} - \tfrac{5}{6} b_{i+1} - \tfrac{1}{24} b_{i+2} - \tfrac{3}{4} b_i \quad .$$
$$m_{i,i+1} = \tfrac{1}{6} b_{i-1} + \tfrac{1}{6} b_{i+2} + \tfrac{1}{2} b_i + \tfrac{1}{2} b_{i+1}$$
$$m_{i,i+2} = \tfrac{1}{6} b_{i+1} - \tfrac{1}{8} b_i - \tfrac{1}{8} b_{i+2}$$

The boundary closure of $M^{(b)}$ (given by a 6×6 matrix) is presented in [41]. (The coefficients fill almost a page.)

The upper part of N,

$$
\begin{array}{lll}
N_{1,1} = \frac{5762947}{2316384} & N_{2,3} = -\frac{2735053}{289548} & N_{3,6} = -\frac{10195}{144774} \\[4pt]
N_{1,2} = -\frac{6374287}{1158192} & N_{2,4} = \frac{273109}{165456} & N_{4,4} = \frac{3259225}{579096} \\[4pt]
N_{1,3} = \frac{573947}{165456} & N_{2,5} = \frac{83767}{1158192} & N_{4,5} = -\frac{324229}{72387} \\[4pt]
N_{1,4} = -\frac{124637}{289548} & N_{2,6} = \frac{245549}{2316384} & N_{4,6} = \frac{1847891}{1158192} \\[4pt]
N_{1,5} = \frac{67979}{2316384} & N_{3,3} = \frac{5266855}{579096} & N_{5,5} = \frac{2626501}{330912} \\[4pt]
N_{1,6} = -\frac{60257}{1158192} & N_{3,4} = -\frac{1099715}{289548} & N_{5,6} = -\frac{7115491}{1158192} \\[4pt]
N_{2,2} = \frac{30392389}{2316384} & N_{3,5} = \frac{869293}{1158192} & N_{6,6} = \frac{21383077}{2316384}
\end{array}
$$

Appendix B.3. Sixth order case.

The boundary derivative operators are given by

$$d_{1;1}v = \frac{-25v_1 + 48v_2 - 36v_3 + 16v_4 - 3v_5}{12\,h}, \qquad d_{1;m}v = \frac{+25v_m - 48v_{m-1} + 36v_{m-2} - 16v_{m-3} + 3v_{m-4}}{12\,h}$$

$$d_{2;1}v = \frac{35v_1 - 104v_2 + 114v_3 - 56v_4 + 11v_5}{12\,h^2}, \qquad d_{2;m}v = \frac{35v_m - 104v_{m-1} + 114v_{m-2} - 56v_{m-3} + 11v_{m-4}}{12\,h^2}$$

$$d_{3;1}v = \frac{-5v_1 + 18v_2 - 24v_3 + 14v_4 - 3v_5}{2\,h^3}, \qquad d_{3;m}v = \frac{+5v_m - 18v_{m-1} + 24v_{m-2} - 14v_{m-3} + 3v_{m-4}}{2\,h^3}$$

The interior scheme of D_4 is given by

$$(D_4 v)_j = \frac{7v_{j-4} - 96v_{j-3} + 676v_{j-2} - 1952v_{j-1} + 2730v_j - 1952v_{j+1} + 676v_{j+2} - 96v_{j+3} + 7v_{j+4}}{240\,h^4}$$

The upper part of the norm H,

$$
\begin{array}{lll}
H_{1,1} = \frac{13649}{43200} & H_{3,3} = \frac{2711}{4320} & H_{5,5} = \frac{7877}{8640} \\[6pt]
H_{2,2} = \frac{12013}{8640} & H_{4,4} = \frac{5359}{4320} & H_{6,6} = \frac{43801}{43200}
\end{array}
$$

The interior stencil of $M^{(b)}$ at row i is given by ($i = 10 \ldots N-9$):

$$m_{i,i-3} = \tfrac{1}{40} b_{i-2} + \tfrac{1}{40} b_{i-1} - \tfrac{11}{360} b_{i-3} - \tfrac{11}{360} b_i$$

$$m_{i,i-2} = \tfrac{1}{20} b_{i-3} - \tfrac{3}{10} b_{i-1} + \tfrac{1}{20} b_{i+1} + \tfrac{7}{40} b_i + \tfrac{7}{40} b_{i-2}$$

$$m_{i,i-1} = -\tfrac{1}{40} b_{i-3} - \tfrac{3}{10} b_{i-2} - \tfrac{3}{10} b_{i+1} - \tfrac{1}{40} b_{i+2} - \tfrac{17}{40} b_i - \tfrac{17}{40} b_{i-1}$$

$$m_{i,i} = \tfrac{1}{180} b_{i-3} + \tfrac{1}{8} b_{i-2} + \tfrac{19}{20} b_{i-1} + \tfrac{19}{20} b_{i+1} + \tfrac{1}{8} b_{i+2} + \tfrac{1}{180} b_{i+3} + \tfrac{101}{180} b_i$$

$$m_{i,i+1} = -\tfrac{1}{40} b_{i-2} - \tfrac{3}{10} b_{i-1} - \tfrac{3}{10} b_{i+2} - \tfrac{1}{40} b_{i+3} - \tfrac{17}{40} b_i - \tfrac{17}{40} b_{i+1}$$

$$m_{i,i+2} = \tfrac{1}{20} b_{i-1} - \tfrac{3}{10} b_{i+1} + \tfrac{1}{20} b_{i+3} + \tfrac{7}{40} b_i + \tfrac{7}{40} b_{i+2}$$

$$m_{i,i+3} = \tfrac{1}{40} b_{i+1} + \tfrac{1}{40} b_{i+2} - \tfrac{11}{360} b_i - \tfrac{11}{360} b_{i+3}$$

The boundary closure of $M^{(b)}$ (given by a 9×9 matrix) is presented in [41]. (The coefficients fill almost a page.)

The upper part of N is given by,

$$N_{1,1} = \frac{1394226315049}{367201486080}$$

$$N_{1,2} = -\frac{1137054563243}{114750464400}$$

$$N_{1,3} = \frac{16614189027367}{1836007430400}$$

$$N_{1,4} = -\frac{1104821700277}{306001238400}$$

$$N_{1,5} = \frac{1355771086763}{1836007430400}$$

$$N_{1,6} = -\frac{27818686453}{459001857600}$$

$$N_{1,7} = -\frac{40671054239}{1836007430400}$$

$$N_{1,8} = \frac{5442887371}{306001238400}$$

$$N_{2,2} = \frac{70616795535409}{2570410402560}$$

$$N_{2,3} = -\frac{173266854731041}{6426026006400}$$

$$N_{2,4} = \frac{28938615291031}{2570410402560}$$

$$N_{2,5} = -\frac{146167361863}{71400288960}$$

$$N_{2,6} = \frac{2793470836571}{12852052012800}$$

$$N_{2,7} = \frac{6219558097}{428401733760}$$

$$N_{2,8} = -\frac{7313844559}{166909766400}$$

$$N_{3,3} = \frac{378613061504779}{12852052012800}$$

$$N_{3,4} - \frac{9117069604217}{642602600640}$$

$$N_{3,5} \frac{632177582849}{233673672960}$$

$$N_{3,6} - \frac{1057776382577}{6426026006400}$$

$$N_{3,7} \frac{443019868399}{4284017337600}$$

$$N_{3,8} - \frac{3707981}{2318191200}$$

$$N_{4,4} = \frac{5029150721885}{514082080512}$$

$$N_{4,5} = -\frac{5209119714341}{1285205201280}$$

$$N_{4,6} = \frac{12235427457469}{12852052012800}$$

$$N_{4,7} = -\frac{13731270505}{64260260064}$$

$$N_{4,8} = \frac{2933596129}{40800165120}$$

$$N_{5,5} = \frac{14871726798559}{2570410402560}$$

$$N_{5,6} = -\frac{7504337615347}{1606506501600}$$

$$N_{5,7} = \frac{310830296467}{171360693504}$$

$$N_{5,8} = -\frac{55284274391}{183600743040}$$

$$N_{6,6} = \frac{106318657014853}{12852052012800}$$

$$N_{6,7} = -\frac{14432772918527}{2142008668800}$$

$$N_{6,8} = \frac{58102695589}{22666758400}$$

$$N_{7,7} = \frac{27102479467823}{2570410402560}$$

$$N_{7,8} = -\frac{1216032192203}{153000619200}$$

$$N_{8,8} = \frac{20799922829107}{1836007430400}$$

References

[1] Saul Abarbanel and Adi Ditkowski. Asymptotically stable fourth-order accurate schemes for the diffusion equation on complex shapes. *Journal of Computational Physics*, 133(2):279 – 288, 1997.

[2] Nathan Albin and Joshua Klarmann. An algorithmic exploration of the existence of high-order summation by parts operators with diagonal norm. *Journal of Scientific Computing*, 69(2):633–650, 2016.

[3] M. Almquist, K. Mattsson, and T. Edvinsson. High-fidelity numerical solution of the time-dependent Dirac equation. *J. Comput. Phys.*, 262:86–103, 2014.

[4] A F Banwell, D R MacAyeal, and O V Sergienko. Breakup of the Larsen B Ice Shelf triggered by chain reaction drainage of supraglacial lakes. *Geophysical Research Letters*, 40(22):5872–5876, 2013.

[5] A F Banwell, I C Willis, G J Macdonald, B Goodsell, D P Mayer, A Powell, and D R MacAyeal. Calving and rifting on the McMurdo Ice Shelf, Antarctica. *Annals of Glaciology*, pages 1–10, 2017.

[6] A. Bayliss, K. E. Jordan, B. J. Lemesurier, and E. Turkel. A fourth order accurate finite difference scheme for the computation of elastic waves. *Bull. Seismol. Soc. Amer.*, 76(4):1115–1132, 1986.

[7] P. D. Boom and D. W. Zingg. High-order implicit time-marching methods based on generalized summation-by-parts operators. *SIAM Journal on Scientific Computing*, 37(6):A2682–A2709, 2015.

[8] P D Bromirski, A Diez, P Gerstoft, R A Stephen, T Bolmer, D A Wiens, R C Aster, and A Nyblade. Ross ice shelf vibrations. *Geophysical Research Letters*, 42(18):7589–7597, 2015.

[9] P D Bromirski, O V Sergienko, and D R MacAyeal. Transoceanic infragravity waves impacting Antarctic ice shelves. *Geophysical Research Letters*, 37(2), 2010.

[10] P D Bromirski and R A Stephen. Response of the Ross Ice Shelf, Antarctica, to ocean gravity-wave forcing. *Annals of Glaciology*, 53(60):163–172, 2012.

[11] PD Bromirski, Z Chen, RA Stephen, P Gerstoft, D Arcas, A Diez, RC Aster, DA Wiens, and A Nyblade. Tsunami and infragravity waves impacting Antarctic ice shelves. *Journal of Geophysical Research*, 2017.

[12] K M Brunt, E A Okal, and D R MacAyeal. Antarctic ice-shelf calving triggered by the Honshu (Japan) earthquake and tsunami, March 2011. *Journal of Glaciology*, 57(205):785–788, 2011.

[13] M. H. Carpenter, D. Gottlieb, and S. Abarbanel. Time-stable boundary conditions for finite-difference schemes solving hyperbolic systems: Methodology and application to high-order compact schemes. *J. Comput. Phys.*, 111(2):220–236, 1994.

[14] David C. Del Rey Fernández, Pieter D. Boom, and David W. Zingg. A generalized framework for nodal first derivative summation-by-parts operators. *J. Comput. Phys.*, 266:214–239, June 2014.

[15] B.A. Erickson and J. Nordström. High order accurate adaptive schemes for long time, highly intermittent geophysics problems. *Journal of Computational and Applied Mathematics*, 271:328 – 338, 2014.

[16] C Fox and V A Squire. Coupling between the ocean and an ice shelf. *Annals of Glaciology*, 15:101–108, 1991.

[17] Th P Gerostathis, KA Belibassakis, and GA Athanassoulis. 3D hydroelastic analysis of very large floating bodies over variable bathymetry regions. *Journal of Ocean Engineering and Marine Energy*, 2(2):159–175, 2016.

[18] P Gerstoft, P Bromirski, Z Chen, R A Stephen, R C Aster, D A Wiens, and A Nyblade. Tsunami excitation of the Ross Ice Shelf, Antarctica. *Journal of the Acoustical Society of America*, 141(5):3526–3526, 2017.

[19] A.E. Gill. *Atmosphere-Ocean Dynamics*. International Geophysics. Elsevier Science, 1982.

[20] P.J.P. Gonalves, M.J. Brennan, and S.J. Elliott. Numerical evaluation of high-order modes of vibration in uniform euler-bernoulli beams. *Journal of Sound and Vibration*, 301(3?5):1035 – 1039, 2007.

[21] B. Gustafsson, H.-O. Kreiss, and J. Oliger. *Time dependent problems and difference methods*. John Wiley & Sons, Inc., 1995.

[22] B. Gustafsson, H.O. Kreiss, and J. Oliger. *Time-Dependent Problems and Difference Methods*. Pure and Applied Mathematics: A Wiley Series of Texts, Monographs and Tracts. Wiley, 2013.

[23] Jan S. Hesthaven. A stable penalty method for the compressible Navier-Stokes equations: III. multidimensional domain decomposition schemes. *SIAM Journal on Scientific Computing*, 20:62–93, 1998.

[24] J.E. Hicken. Output error estimation for summation-by-parts finite-difference schemes. *Journal of Computational Physics*, 231(9):3828 – 3848, 2012.

[25] G Holdsworth and J Glynn. Iceberg calving from floating glaciers by a vibrating mechanism. *Nature*, 274(5670):464–466, 1978.

[26] H.-O. Kreiss and G. Scherer. Finite element and finite difference methods for hyperbolic partial differential equations. *Mathematical Aspects of Finite Elements in Partial Differential Equations., Academic Press, Inc.*, 1974.

[27] Heinz-Otto Kreiss and Joseph Oliger. Comparison of accurate methods for the integration of hyperbolic equations. *Tellus*, XXIV:199–215, 1972.

[28] P K Kundu and I M Cohen. *Fluid Mechanics*. Elsevier, 2008.

[29] H Lamb. *Hydrodynamics*. Cambridge University Press, 1932.

[30] L. D. Landau and E. M. Lifshitz. *Theory of Elasticity*. Course of Theoretical Physics. Elsevier, New York, 1986.

[31] S. K. Lele. Compact finite difference schemes with spectral-like resolution. *J. Comput. Phys.*, 103:16–42, 1992.

[32] G C Lotto and E M Dunham. High-order finite difference modeling of tsunami generation in a compressible ocean from offshore earthquakes. *Computational Geosciences*, 19(2):327–340, 2015.

[33] Tomas Lundquist and Jan Nordström. The sbp-sat technique for initial value problems. *Journal of Computational Physics*, 270(0):86 – 104, 2014.

[34] K. Mattsson, M. Almquist, and M. H. Carpenter. Optimal diagonal-norm SBP operators. *J. Comput. Phys.*, 264:91–111, 2014.

[35] K. Mattsson and M. H. Carpenter. Stable and accurate interpolation operators for high-order multi-block finite-difference methods. *SIAM J. Sci Comput.*, 32(4):2298–2320, 2010.

[36] K. Mattsson, F. Ham, and G. Iaccarino. Stable and accurate wave propagation in discontinuous media. *J. Comput. Phys.*, 227:8753–8767, 2008.

[37] K. Mattsson and J. Nordström. Summation by parts operators for finite difference approximations of second derivatives. *J. Comput. Phys.*, 199(2):503–540, 2004.

[38] K. Mattsson and J. Nordström. High order finite difference methods for wave propagation in discontinuous media. *J. Comput. Phys.*, 220:249–269, 2006.

[39] K. Mattsson and F. Parisi. Stable and accurate second-order formulation of the shifted wave equation. *Commun. Comput. Phys.*, 7:103–137, 2010.

[40] K. Mattsson, M. Svärd, and M. Shoeybi. Stable and accurate schemes for the compressible navier-stokes equations. *J. Comput. Phys.*, 227(4):2293–2316, 2008.

[41] Ken Mattsson. Summation by parts operators for finite difference approximations of second-derivatives with variable coefficients. *Journal of Scientific Computing*, 51:650–682, 2012.

[42] Ken Mattsson. Diagonal-norm summation by parts operators for finite difference approximations of third and fourth derivatives. *J. Comput. Phys.*, 274(0):432 – 454, 2014.

[43] Ken Mattsson. Diagonal-norm upwind SBP operators. *Journal of Computational Physics*, 335:283 – 310, 2017.

[44] Ken Mattsson and Vidar Stiernström. High-fidelity numerical simulation of the dynamic beam equation. *Journal of Computational Physics*, 286(0):194 – 213, 2015.

[45] Ken Mattsson and Jonatan Werpers. High-fidelity numerical simulation of solitons in the nerve axon. *Journal of Computational Physics*, 305:793 – 816, 2016.

[46] Anna Nissen, Katharina Kormann, Magnus Grandin, and Kristoffer Virta. Stable difference methods for block-oriented

27

adaptive grids. *Journal of Scientific Computing*, 65(2):486–511, 2015.

[47] Jan Nordstrm and Tomas Lundquist. Summation-by-parts in time. *Journal of Computational Physics*, 251(Supplement C):487 – 499, 2013.

[48] P. Olsson. Summation by parts, projections, and stability I. *Math. Comp.*, 64:1035, 1995.

[49] P. Olsson. Summation by parts, projections, and stability II. *Math. Comp.*, 64:1473, 1995.

[50] T. K. Papathanasiou, A. E. Karperaki, E. E. Theotokoglou, and K. A. Belibassakis. Hydroelastic analysis of ice shelves under long wave excitation. *Natural Hazards and Earth System Sciences*, 15(8):1851–1857, 2015.

[51] N. Anders Petersson, Ossian O'Reilly, Björn Sjögreen, and Samuel Bydlon. Discretizing singular point sources in hyperbolic wave propagation problems. *Journal of Computational Physics*, 321:532–555, 2016.

[52] S. De Rango and D. W. Zingg. A high-order spatial discretization for turbulent aerodynamic computations. *AIAA J.*, 39(7):1296–1304, 2001.

[53] Søren S.L. Andersen, Andrew D. Jackson, and Thomas Heimburg. Towards a thermodynamic theory of nerve pulse propagation. *Progress in Neurobiology*, 88(2):104 – 113, 2009.

[54] E Rignot, G Casassa, P Gogineni, W Krabill, A Rivera, and R Thomas. Accelerated ice discharge from the Antarctic Peninsula following the collapse of Larsen B ice shelf. *Geophysical Research Letters*, 31(18), 2004.

[55] T Scambos, H A Fricker, C-C Liu, J Bohlander, J Fastook, A Sargent, R Massom, and A-M Wu. Ice shelf disintegration by plate bending and hydro-fracture: Satellite observations and model results of the 2008 Wilkins ice shelf break-ups. *Earth and Planetary Science Letters*, 280(1):51–60, 2009.

[56] T A Scambos, JA Bohlander, CA Shuman, and P Skvarca. Glacier acceleration and thinning after ice shelf collapse in the Larsen B embayment, Antarctica. *Geophysical Research Letters*, 31(18), 2004.

[57] C C L Sells. The effect of a sudden change of shape of the bottom of a slightly compressible ocean. *Philosophical Transactions of the Royal Society of London A: Mathematical, Physical and Engineering Sciences*, 258(1092):495–528, 1965.

[58] OV Sergienko. Elastic response of floating glacier ice to impact of long-period ocean waves. *Journal of Geophysical Research*, 115(F4), 2010.

[59] OV Sergienko. Behavior of flexural gravity waves on ice shelves: Application to the ross ice shelf. *Journal of Geophysical Research: Oceans*, 2017.

[60] V A Squire, J P Dugan, P Wadhams, P J Rottier, and A K Liu. Of ocean waves and sea ice. *Annual Review of Fluid Mechanics*, 27(1):115–168, 1995.

[61] VA Squire. Of ocean waves and sea-ice revisited. *Cold Regions Science and Technology*, 49(2):110–133, 2007.

[62] J J Stoker. *Water waves: The mathematical theory with applications*, volume 36. John Wiley & Sons, 2011.

[63] B. Strand. Summation by parts for finite difference approximations for d/dx. *J. Comput. Physics*, 110:47–67, 1994.

[64] John C. Strikwerda. High-order-accurate schemes for incompressible viscous flow. *International Journal for Numerical Methods in Fluids*, 24:715–734, 1997.

[65] Izolda V Sturova. Time-dependent response of a heterogeneous elastic plate floating on shallow water of variable depth. *Journal of Fluid Mechanics*, 637:305–325, 2009.

[66] J Tollefson. Giant crack in Antarctic ice shelf spotlights advances in glaciology. *Nature*, 542(7642):402–403, 2017.

[67] S.M. Wiedemann. Natural frequencies and mode shapes of arbitrary beam structures with arbitrary boundary conditions. *Journal of Sound and Vibration*, 300(1–2):280 – 291, 2007.